JM PAPERS

Equilibrium distributions under advection–diffusion in laminar channel flow with partially absorbing boundaries

Tomás Aquino†

Spanish National Research council (IDAEA – CSIC), 08034 Barcelona, Spain

Advective–diffusive transport in Poiseuille flow through a channel with partially absorbing walls is a classical problem with applications to a broad range of natural and engineered scenarios, ranging from solute and heat transport in porous and fractured media to absorption in biological systems and chromatography. We study this problem from the perspective of transverse distributions of surviving mass and velocity, which are a central ingredient of recent stochastic models of transport based on the sampling of local flow velocities along trajectories. We show that these distributions tend to asymptotic equilibria for large times and travel distances, and derive rigorous explicit expressions for arbitrary reaction rate. We find that the equality of flux-weighted and breakthrough distributions that holds for conservative transport breaks in the presence of reaction, and that the average velocity of the scalar plume is no longer fully characterized by the transverse distribution of flow velocities sampled at a given time.

Key words: laminar reacting flows, dispersion

1. Introduction

Transport in Poiseuille flow within a channel is a classical problem that has served to advance the understanding of the fundamental features of advection–dispersion of scalars such as solutes and temperature, going back to the classical works on asymptotic dispersion of Taylor ([1953](#)) and Aris ([1956](#)). Partially absorbing channel walls, where a transported scalar that diffuses into the walls is consumed proportionally to its local concentration, can represent a variety of physical processes, such as reactive solute consumption or sorption in porous or fractured media (Battiato *et al.* [2011](#)), heat transport in pipes, rock fractures

† Email address for correspondence: tomas.aquino@idaea.csic.es

or other conduits (Lungu & Moffatt 1982), absorption in biological tissues (Davidson & Schroter 1983), and chromatography (Sankarasubramanian & Gill 1973; Balakotaiah, Chang & Smith 1995). In what follows, we adopt the language of reactive solute transport for concreteness and ease of exposition.

Traditionally, the conservative problem is treated in terms of the method of moments (Aris 1956), in which differential equations can be derived for successively higher moments along the longitudinal (mean flow) direction, averaged along the transverse direction(s). In addition to asymptotic mean velocities and dispersion coefficients, the evolution of the longitudinal plume towards normality can also be quantified using this type of approach (Chatwin 1970). The question of how surface reaction affects effective advective velocities and dispersion has received much attention (Sankarasubramanian & Gill 1973; De Gance & Johns 1978*b*; Lungu & Moffatt 1982; Shapiro & Brenner 1986; Balakotaiah *et al.* 1995; Mikelić, Devigne & Van Duijn 2006; Biswas & Sen 2007). Sankarasubramanian & Gill (1973), followed by De Gance & Johns (1978*a*,*b*), generalized the asymptotic theory of Taylor (1953) and Aris (1956) to the case of absorbing walls, and computed dispersive approximations to the longitudinal concentration field. A treatment in terms of series expansions of the longitudinal moments in Fourier space is given by Lungu & Moffatt (1982). These works derive differential equations for longitudinal moments at asymptotic times, and in particular give a detailed account of effective plume velocities and dispersion coefficients. Intuitively, solute removal preferentially depletes low-velocity areas, and these works quantify the corresponding increase in average plume velocity, as well as the reduction in dispersion due to the associated decrease in the variability of sampled velocities. Later, Barton (1984) derived a general framework for computing the time-dependent moments and asymptotic solutions based on eigenfunction expansions, extending his previous work (Barton 1983) and that of Chatwin (1970) for the conservative problem. More recently, a stochastic formulation was developed by Biswas & Sen (2007). Although we focus here on a linear, irreversible reaction, we note that when forward reaction is accompanied by the reverse reaction, such as in chromatographic applications where sorption is accompanied by desorption, the net effect at late times is a decrease in plume velocity characterized by a retardation factor associated with the average time that the solute remains sorbed to the channel walls (Paine, Carbonell & Whitaker 1983; Balakotaiah *et al.* 1995; Jiang *et al.* 2022). These two scenarios and the time scales governing the different regimes can be reconciled within a unified description (Zhang, Hesse & Wang 2017). The linear irreversible picture applies, for example, over time scales where the reverse reaction may be neglected and local surface reactant concentrations may be approximated as constant, or when thermally conducting walls may be approximated as a thermal reservoir.

Despite these significant advances, previous work has focused mainly on the transverse-averaged moments and resulting approximations for the longitudinal concentration field. The present work offers a fresh perspective on this classical problem from the point of view of transverse mass and velocity distributions. The work of Barton (1984) provides a formal means to compute the dependency of longitudinal moments on transverse position and has been used to analyse the evolution of transverse averages and breakthrough curves (Yasuda 1984; Guan & Chen 2024). Here, we provide an alternative approach to analyse the asymptotic transverse variability in plume concentrations and advective velocities directly and in detail. Transverse distributions are relevant in the current context due to their fundamental role in spatial Markov models of transport in heterogeneous systems, which describe transport in terms of a stochastic evolution of velocities along solute trajectories over fixed spatial increments (Le Borgne, Dentz

& Carrera 2008; Dentz *et al.* 2016; Sherman *et al.* 2019, 2021; Puyguiraud, Gouze & Dentz 2021; Aquino & Le Borgne 2021*b*). Recent theoretical, numerical and experimental advances regarding flow and transport in biological systems such as lung tissue (Sznitman 2021) and blood vessel networks in the brain (Goirand, Le Borgne & Lorthois 2021) and tumours (Dewhirst & Secomb 2017) underline the importance of transport and surface exchange for processes ranging from drug delivery to oxygen uptake and metabolic waste disposal. The question of how surface reaction modifies velocity distributions across solute plumes is thus central for the development of upscaled models of reactive transport in natural subsurface systems and other heterogeneous media.

We first address the following question: does the transverse distribution of solute concentrations, normalized by surviving mass, admit an asymptotic form for large times and travel distances from a given initial condition? We find that the answer is affirmative, and we derive explicit expressions for equilibrium mass, velocity and breakthrough distributions for arbitrary reaction rate. To characterize breakthrough distributions, it turns out to be necessary to determine the asymptotic mean plume velocity. To this end, we provide an analysis that highlights the role of subleading transverse variability in the mean plume position, while reproducing previous results based on the method of moments (Lungu & Moffatt 1982; Barton 1984). We show in particular that the equality of flux-weighted (i.e. weighted by local velocities) and breakthrough (i.e. associated with flux over a control plane) distributions that has been established for conservative transport (Dentz *et al.* 2016; Puyguiraud *et al.* 2021) breaks down in the presence of reaction, and that the mean plume velocity as a function of time is no longer fully characterized by the transverse distribution of flow velocities sampled by the plume at a given time. The extent of these effects depends on medium geometry and is more pronounced for flow in a cylindrical channel than between parallel plates.

The paper is organized as follows. In § 2, we formalize the problem and present the governing equations. In § 3, we introduce the transverse distributions and related average quantities that we then compute and compare to simulations for large times and travel distances in § 4, in both two dimensions (flow between parallel plates) and three dimensions (flow in a cylindrical channel). Section 5 presents an overall discussion and conclusions. Ancillary details and derivations can be found in the appendices.

2. Transport in a channel with reactive walls

Consider Poiseuille flow through an infinite channel of fixed cross-section, and a solute undergoing advective–diffusive transport within the channel. We begin by introducing some notation. We denote the channel by Ω and an arbitrary cross-section by $\Omega_\perp$, and the channel radius by a (half-width in two dimensions). We consider a Cartesian coordinate system with the origin at the channel centre and such that x is oriented along the channel. We denote spatial positions by $\boldsymbol{x} = (x, \boldsymbol{x}_\perp) \in \Omega$, with $\boldsymbol{x}_\perp \in \Omega_\perp$ equal to y in two dimensions and to (y, z) in three dimensions. We use the notation $|\Lambda|$ applied to a d_Λ-dimensional spatial domain Λ to denote its d_Λ-dimensional measure (volume for $d_\Lambda = 3$, area for $d_\Lambda = 2$, and number of points for $d_\Lambda = 1$). For example, the cross-sectional area is given by $|\Omega_\perp| = \pi a^2$ for a cylindrical channel in three dimensions ($\Omega_\perp$ has dimension two, so $|\Omega_\perp|$ is an area) and $|\Omega_\perp| = 2a$ for two spatial dimensions ($|\Omega_\perp|$ is a length). Finally, we denote partial derivatives with respect to a variable ξ by ∂_ξ.

Within the channel, $\boldsymbol{x} \in \Omega$, solute concentrations obey the advection–dispersion equation

$$\partial_t c(\boldsymbol{x}; t) = v_E(\boldsymbol{x}_\perp) \, \partial_x c(\boldsymbol{x}; t) + D \, \nabla^2 c(\boldsymbol{x}; t), \tag{2.1}$$

985 A16-3

where t is time, D is the diffusion coefficient, and for stratified, fully-developed channel flow, the spatial (Eulerian) velocity profile $v_E(\boldsymbol{x}_\perp)$ is a function of $\boldsymbol{x}_\perp \in \Omega_\perp$ only:

$$v_E(\boldsymbol{x}_\perp) = v_M \left(1 - \frac{|\boldsymbol{x}_\perp|^2}{a^2} \right), \tag{2.2}$$

where v_M is the maximum velocity, attained at the centre of the channel ($\boldsymbol{x}_\perp = 0$). We define the Péclet number as

$$Pe = \frac{a \, \overline{v_E}}{D}, \tag{2.3}$$

where

$$\overline{v_E} = |\Omega_\perp|^{-1} \int_{\Omega_\perp} \mathrm{d}\boldsymbol{x}_\perp \, v_E(\boldsymbol{x}_\perp) \tag{2.4}$$

is the Eulerian mean velocity.

Solute diffusion coefficients in both environmental and engineering applications are commonly in the range 10^{-10}–10^{-9} m^2 s^{-1}, whereas common flow rates and relevant length scales (such as the pore, pipe or blood vessel diameter, or the fracture aperture) vary substantially and are often not independent. For example, subsurface flows through porous and fractured media usually range from approximately $Pe = 10^{-2}$ to $Pe = 10^4$, with advection-dominated conditions ($Pe > 1$) being common, in particular in fractures (de Marsily 1986). In chromatography, the Péclet number is usually between unity and a few hundred (Gritti & Guiochon 2013), although it should be noted that turbulent effects may be non-negligible in engineering applications such as chromatography and flow cell batteries. Typical flow rates in blood capillary networks (Ivanov, Kalinina & Levkovich 1981) are of the order of mm s^{-1}, with vessel diameters of the order of μm, corresponding to a typical Pe of approximately 1–10. For heat transport in fractures, the thermal diffusivity is commonly approximately 10^{-7} m^2 s, and $Pe \sim 10$–10^2 (de Marsily 1986).

The cross-section concentration, obtained by integrating out the longitudinal coordinate x, is

$$c_\perp(\boldsymbol{x}_\perp; t) = \int_{-\infty}^{\infty} \mathrm{d}x \, c(\boldsymbol{x}; t). \tag{2.5}$$

Within $\Omega_\perp$, the cross-section concentration obeys the diffusion equation

$$\partial_t c_\perp(\boldsymbol{x}_\perp; t) = D \, \nabla_\perp^2 c_\perp(\boldsymbol{x}_\perp; t), \tag{2.6}$$

which can be verified by integrating out x in (2.1), and applying natural boundary conditions at $x = \pm\infty$, i.e. setting the limit as $|x| \to \infty$ of c and its derivative to zero, which is needed to ensure finite mass in an infinite domain. Here and throughout, $\nabla_\perp$ represents the gradient with respect to the transverse coordinates. We consider this problem subject to a given initial condition $c_\perp(\boldsymbol{x}_\perp; 0)$, which is determined from the initial concentration field $c(\boldsymbol{x}; 0)$ according to (2.5).

Surface reaction can be represented through the boundary conditions. Linear depletion at a constant surface rate k_A $[LT^{-1}]$ corresponds to partially absorbing boundaries, i.e. the Robin boundary conditions

$$\boldsymbol{n}_\perp(\boldsymbol{x}_\perp) \cdot D \, \nabla_\perp c_\perp(\boldsymbol{x}_\perp; t) = -k_A \, c_\perp(\boldsymbol{x}_\perp; t), \quad \boldsymbol{x}_\perp \in \partial\Omega_\perp, \tag{2.7}$$

where $\boldsymbol{n}_\perp(\boldsymbol{x}_\perp)$ is the outward normal at the point $\boldsymbol{x}_\perp$ on the boundary $\partial\Omega_\perp$. For the conservative problem, $k_A = 0$, this reduces to a reflecting boundary, $\boldsymbol{n}_\perp \cdot \nabla_\perp c_\perp|_{\partial\Omega_\perp} = 0$,

while for instantaneous reaction, $k_A \to \infty$, we have a fully absorbing boundary, $c_\perp|_{\partial\Omega_\perp} = 0$. We define the Damköhler number Da as the ratio of the characteristic diffusion and reaction times τ_D and τ_R associated with the channel radius a:

$$Da = \frac{\tau_D}{\tau_R} = \frac{ak_A}{2D}, \quad \tau_D = \frac{a^2}{2D}, \quad \tau_R = \frac{a}{k_A}. \tag{2.8a–c}$$

Because the reaction rate k_A depends on both the thermodynamics of the reaction and the surface concentrations of reactants at the interface, the Damköhler number for solute transport problems can vary over a very broad range of orders of magnitude. For heat transport, we have $Da = aH/(2K)$, where H is the surface conductance or heat transfer coefficient, and K is the thermal conductivity of the surface (Carslaw & Jaeger 1986). For example, for subsurface transport in fractured rock, we have $K \sim$ W m^{-1} K^{-1} (Carslaw & Jaeger 1986) and $H \sim 10$–10^2 W m^{-2} K^{-1} (Heinze 2021), so that, using $a \sim 10^{-6}$–10^{-2} m, we estimate typical values of Da in the range 10^{-5}–1.

It has been established that as for the traditional conservative problem (Taylor 1953; Aris 1956), the concentration plume for the reactive problem approaches a Gaussian shape along the longitudinal direction at late times (Chatwin 1970; Biswas & Sen 2007). The effective (Taylor) dispersion coefficient is then given by

$$D_e = D(1 + \eta\, Pe^2), \tag{2.9}$$

where η is a dimensionless constant that depends on the domain geometry and decreases monotonically with Da, quantifying the decrease in longitudinal dispersion due to the reduced variability in sampled velocities (Lungu & Moffatt 1982). For the two-dimensional (2-D) channel, $\eta = 2/105 \approx 1.9 \times 10^{-2}$ for the conservative problem, and $\eta = 9\pi^{-6}(75\pi^2 - \pi^4 - 630)/45 \approx 2.7 \times 10^{-3}$ for $Da \to \infty$. The corresponding values for the three-dimensional (3-D) problem are $\eta = 1/48 \approx 2.1 \times 10^{-2}$ and $\eta \approx 5.0 \times 10^{-3}$.

3. Transverse distributions

In this section, we introduce different probability density functions (p.d.f.s) of interest across the transverse direction, before proceeding to discuss the corresponding asymptotic equilibria in §4. In Appendix A, we discuss how these quantities can be represented in terms of concentration moments in the classical Aris–Barton formulation (Barton 1984).

3.1. *Surviving mass*

The total mass at time t can be expressed as

$$M(t) = \int_\Omega \mathrm{d}\boldsymbol{x}\, c(\boldsymbol{x}; t) = \int_{\Omega_\perp} \mathrm{d}\boldsymbol{x}_\perp\, c_\perp(\boldsymbol{x}_\perp; t). \tag{3.1}$$

We use the notation $\int_\Omega \mathrm{d}\boldsymbol{x} = \int \mathrm{d}x \int \mathrm{d}y \int \mathrm{d}z$ for multi-dimensional integrals. For $M(t) \neq 1$, $c_\perp(\cdot; t)$ is a density, but not a p.d.f., because it is not normalized to unit integral. The p.d.f. $p_t(\cdot; t)$ of surviving mass, which describes the transverse mass profile along the

cross-section at time *t*, is given by

$$p_t(\boldsymbol{x}_\perp; t) = \frac{c_\perp(\boldsymbol{x}_\perp; t)}{M(t)}. \tag{3.2}$$

If it exists, the corresponding equilibrium p.d.f. is

$$p_t^\infty(\boldsymbol{x}_\perp) = \lim_{t \to \infty} p_t(\boldsymbol{x}_\perp; t). \tag{3.3}$$

3.2. *Velocity at fixed time*

A velocity p.d.f. describes the probability density of encountering a certain velocity in a spatial domain, sampled according to some prescribed distribution. For the flow profile (2.2), we may disregard the longitudinal direction and consider only the cross-section. We first introduce the Eulerian velocity p.d.f. p_E, which is defined as the probability density associated with finding a certain velocity magnitude value at a uniformly random spatial location. We also define the flux-weighted Eulerian p.d.f.

$$p_F(v) = \frac{v\, p_E(v)}{\overline{v_E}}, \tag{3.4}$$

where the Eulerian mean velocity, defined in (2.4), obeys $\overline{v_E} = \int_0^{v_M} \mathrm{d}v\, v\, p_E(v)$. We denote the flux-weighted mean velocity by

$$\overline{v_F} = \int_0^{v_M} \mathrm{d}v\, v\, p_F(v) = |\Omega_\perp|^{-1} \int_{\Omega_\perp} \mathrm{d}\boldsymbol{x}_\perp \frac{v_E^2(\boldsymbol{x}_\perp)}{\overline{v_E}}. \tag{3.5}$$

The transverse velocity p.d.f. at fixed time, $p_{v_t}(\cdot; t)$, is obtained by sampling spatial locations according to the p.d.f. $p_t(\cdot; t)$, which describes the probability density of surviving mass at a given time as a function of cross-section positions, rather than uniformly. If p_t^∞ exists, then this velocity p.d.f. also admits an equilibrium given by

$$p_{v_t}^\infty(v) = |\Omega_\perp|\, p_t^\infty[r_\perp(v)]\, p_E(v), \tag{3.6}$$

where

$$r_\perp(v) = a\sqrt{1 - \frac{v}{v_M}} \tag{3.7}$$

are the radial distances from the channel centre where the velocity magnitude equals v for the Poiseuille flow profile (2.2). Here and in similar contexts, we use the slight abuse of notation $p_t^\infty[r_\perp(v)] = p_t^\infty(\boldsymbol{x}_\perp)|_{|\boldsymbol{x}_\perp| = r_\perp(v)}$ for convenience. Note that $p_{v_t}^\infty$ reduces to the Eulerian p.d.f. p_E if $p_t^\infty(\boldsymbol{x}_\perp) = 1/|\Omega_\perp|$, i.e. if mass is distributed uniformly along the cross-section. Further details on the Eulerian and flux-weighted Eulerian p.d.f.s, including table 2 summarizing useful quantities and a derivation of (3.6), are given in Appendix B.

985 A16-6

The mean velocity associated with $p_{v_t}^\infty$ is

$$v_t^\infty = \int_0^{v_M} \mathrm{d}v \, v \, p_{v_t}^\infty(v) = \int_{\Omega_\perp} \mathrm{d}\boldsymbol{x}_\perp \, v_E(\boldsymbol{x}_\perp) \, p_t^\infty(\boldsymbol{x}_\perp). \tag{3.8}$$

Finally, we introduce the fixed-time flux-weighted velocity p.d.f., corresponding to assigning a weight proportional to the local velocity to the sampling of spatial locations:

$$p_{v_t,F}^\infty(v) = |\Omega_\perp| \, p_{t,F}^\infty[r_\perp(v)] \, p_E(v) = |\Omega_\perp| \, p_t^\infty[r_\perp(v)] \, \frac{\overline{v_E} \, p_F(v)}{v_t^\infty}, \tag{3.9}$$

where the spatial sampling p.d.f. is obtained by flux-weighting the surviving mass p.d.f. (3.3):

$$p_{t,F}^\infty(\boldsymbol{x}_\perp) = \frac{v_E(\boldsymbol{x}_\perp) \, p_t^\infty(\boldsymbol{x}_\perp)}{v_t^\infty}. \tag{3.10}$$

The relationship between these p.d.f.s and solute breakthrough over a control plane is discussed in § 3.3. The associated mean velocity is

$$v_{t,F}^\infty = \int_0^{v_M} \mathrm{d}v \, v \, p_{v_t,F}^\infty(v) = \frac{1}{v_t^\infty} \int_{\Omega_\perp} \mathrm{d}\boldsymbol{x}_\perp \, v_E^2(\boldsymbol{x}_\perp) \, p_t^\infty(\boldsymbol{x}_\perp). \tag{3.11}$$

One might reasonably suppose the asymptotic mean of the fixed-time velocity p.d.f., v_t^∞ (3.8), to correspond to the asymptotic mean velocity of the solute plume at large fixed times. While this is true for conservative transport (Dentz *et al.* 2016), it is in fact not the case for the reactive problem. To see why, first recall that the mean plume velocity $v_P(t)$ as a function of time is defined as the rate of change of the mean plume position $m_P(t)$, which is given by

$$m_P(t) = M^{-1}(t) \int_\Omega \mathrm{d}\boldsymbol{x} \, x \, c(\boldsymbol{x}, t). \tag{3.12}$$

Taking the time derivative gives

$$v_P(t) = M^{-1}(t) \int_\Omega \mathrm{d}\boldsymbol{x} \, x \, \partial_t c(\boldsymbol{x}, t) + \alpha(t) \, m_P(t), \tag{3.13}$$

where $\alpha = M^{-1} |\mathrm{d}M/\mathrm{d}t|$ is the effective reaction rate across the solute plume (units of inverse time). Integrating the advection–dispersion equation (ADE) (2.1) in Ω and assuming that the equilibrium distribution p_t^∞ exists, we find that the late-time effective rate is constant:

$$\lim_{t \to \infty} \alpha(t) = \alpha^\infty = k_A \, |\partial\Omega_\perp| \, p_t^\infty(\boldsymbol{x}_\perp \in \partial\Omega_\perp). \tag{3.14}$$

Again using the ADE (2.1) to substitute for $\partial_t c(\boldsymbol{x}, t)$ in (3.13) and performing the appropriate integrations, we find for late times that

$$v_P(t) = v_t^\infty + \alpha^\infty \left[m_P(t) - m_W(t) \right], \tag{3.15}$$

where

$$m(\boldsymbol{x}_\perp, t) = \frac{\displaystyle\int_{-\infty}^\infty \mathrm{d}x \, x \, c(\boldsymbol{x}, t)}{\displaystyle\int_{-\infty}^\infty \mathrm{d}x \, c(\boldsymbol{x}, t)} = \frac{\displaystyle\int_{-\infty}^\infty \mathrm{d}x \, x \, c(\boldsymbol{x}, t)}{M(t) \, p_t^\infty(\boldsymbol{x}_\perp)}, \quad m_W(t) = m(\boldsymbol{x}_\perp \in \partial\Omega_\perp, t) \tag{3.16a,b}$$

are the mean longitudinal plume positions given an arbitrary transverse position $\boldsymbol{x}_\perp$ and a position $\boldsymbol{x}_\perp$ at the channel walls, respectively.

Reactive consumption cannot lead to a maximum velocity larger than v_M, the centre-channel velocity. However, according to (3.15), if $m_P(t) - m_W(t)$ grew asymptotically as time $t \to \infty$, so would the mean plume velocity $v_P(t)$. Thus $m_P(t) - m_W(t)$ must be at most constant at late times, and we find from (3.15) that $v_P(t)$ is constant at late times. For the conservative problem, it is well known that the mean plume velocity approaches the Eulerian mean velocity $\overline{v_E}$. Since reaction depletes mass in low-velocity regions, the late-time plume velocity must not be smaller than $\overline{v_E}$ and must therefore be non-zero, so that $m_P(t)$ must grow asymptotically. Then the fact that $m_P(t) - m_W(t)$ cannot grow at late times implies $m_P(t) = m_W(t)$ to leading order. On the other hand, by definition, $v_P(t) = dm_P(t)/dt$, and we conclude that to leading order $v_P(t) = dm_W(t)/dt$ also. Therefore, $m_W(t) \sim v_P^\infty t$ asymptotically, with the equilibrium mean plume velocity given by

$$v_P^\infty = \lim_{t \to \infty} \frac{dm_W(t)}{dt} = \lim_{t \to \infty} \frac{m_W(t)}{t}. \tag{3.17}$$

As we will show below, it turns out that $v_P^\infty \geq v_t^\infty \geq \overline{v_E}$, where the equalities hold only for the conservative problem. This may also be seen using the more traditional method of moments, which has been used to compute v_P^∞ (Lungu & Moffatt 1982). The present approach clarifies the physical origin of this effect: even though the global mean plume position equals the mean plume position at the wall to leading order at late times, the subleading difference of these quantities contributes at leading order to the asymptotic mean plume velocity in (3.15).

In order to compute v_P^∞ below, we consider the auxiliary quantity

$$f(\boldsymbol{x}_\perp, t) = M^{-1}(t) \int_{-\infty}^\infty dx\, x\, c(\boldsymbol{x}, t). \tag{3.18}$$

From this definition, we have at late times

$$m(\boldsymbol{x}_\perp, t) = \frac{f(\boldsymbol{x}_\perp, t)}{p_t^\infty(\boldsymbol{x}_\perp)}, \quad m_P(t) = \int_{\Omega_\perp} d\boldsymbol{x}_\perp f(\boldsymbol{x}_\perp, t). \tag{3.19a,b}$$

Multiplying the ADE (2.1) by $x/M(t)$, integrating out x, and rearranging terms, we obtain an evolution equation for f. At late times, it reads

$$\partial_t f(\boldsymbol{x}_\perp, t) = D \nabla_\perp^2 f(\boldsymbol{x}_\perp, t) + \alpha^\infty f(\boldsymbol{x}_\perp, t) + v_E(\boldsymbol{x}_\perp) p_t^\infty(\boldsymbol{x}_\perp), \tag{3.20}$$

with the reactive boundary condition (2.7) applied to f, and an initial condition $f(\boldsymbol{x}_\perp, 0)$ determined by the initial concentration field according to (3.18). This equation has the form of the transverse ADE (2.6) in terms of differential operators, but with an additional linear production term at rate α^∞, and a source term given by the velocity field weighted by the surviving mass distribution. We will analyse the late-time behaviour of (3.20) in more detail separately for the 2-D and 3-D channels in what follows. In particular, we will find that

$$m(\boldsymbol{x}_\perp, t) = v_P^\infty t + \Delta m(\boldsymbol{x}_\perp), \tag{3.21}$$

where the constant-in-time mean-position discrepancy at late times $\Delta m(\boldsymbol{x}_\perp)$ obeys

$$\int_{\Omega_\perp} d\boldsymbol{x}_\perp p_t^\infty(\boldsymbol{x}_\perp) \Delta m(\boldsymbol{x}_\perp) - \Delta m_W = \lim_{t \to \infty} [m_P(t) - m_W(t)] = \frac{v_P^\infty - v_t^\infty}{\alpha^\infty}, \tag{3.22}$$

where $\Delta m_W = \Delta m(\boldsymbol{x}_\perp \in \partial\Omega_\perp)$, so that (3.15) for the mean plume velocity is satisfied.

3.3. *Breakthrough over a fixed control plane*

The breakthrough of mass as a function of time is a standard metric that represents the total advective mass flux passing a control plane at a fixed longitudinal position. Here, we consider breakthrough profiles, by which we mean the profile of the mass flux per area as a function of transverse position over the control plane. As before, we are interested in the existence of equilibrium profiles when normalized by surviving mass. Thus we define the breakthrough p.d.f., i.e. the breakthrough profile normalized by the total mass that crosses a control plane at position x over all times, and we seek its equilibrium form:

$$p_s(\boldsymbol{x}_\perp; x) = \frac{\displaystyle\int_0^\infty \mathrm{d}t\, v_E(\boldsymbol{x}_\perp)\, c(\boldsymbol{x}, t)}{\displaystyle\int_{\Omega_\perp} \mathrm{d}\boldsymbol{x}_\perp \int_0^\infty \mathrm{d}t\, v_E(\boldsymbol{x}_\perp)\, c(\boldsymbol{x}, t)}, \quad p_s^\infty(\boldsymbol{x}_\perp) = \lim_{x \to \infty} p_s(\boldsymbol{x}_\perp; x). \quad (3.23a,b)$$

The advective mass flux is locally proportional to the flow velocity. At large distances, the crossing times are also large, so that we may expect the equilibrium breakthrough p.d.f. to result from flux-weighting the surviving mass p.d.f., i.e. $p_s^\infty = p_{t,F}^\infty$; see (3.10). This is indeed the case for the conservative problem (Dentz *et al.* 2016), but, surprisingly, the equality does not hold exactly for the reactive problem due to the subleading contributions $\Delta m(\boldsymbol{x}_\perp)$ to the mean plume position discussed in the previous subsection (see (3.21)). To see this, consider that, as already discussed, the plume is Gaussian along the longitudinal direction at late times (Chatwin 1970; Biswas & Sen 2007). We thus write the concentration field as

$$c(\boldsymbol{x}, t) = M(t)\, p_t^\infty(\boldsymbol{x}_\perp)\, G[x; v_P^\infty t + \Delta m(\boldsymbol{x}_\perp), 2D_e t], \quad (3.24)$$

where $G(\cdot; \xi, \sigma^2)$ is the Gaussian p.d.f. of mean ξ and variance σ^2, the mean plume position is given by (3.21), and the Taylor dispersion coefficient D_e is given by (2.9). We have established in (3.14) that the mass decays at a constant rate α^∞ at late times, which is equivalent to saying the late-time decay of mass is exponential at rate α^∞. Thus the time integrals in (3.23a) are proportional to the Laplace transform over time of the Gaussian p.d.f. in (3.24) evaluated at α^∞, which, for $x \geq \Delta m(\boldsymbol{x}_\perp)$, is given by

$$\mathcal{L}_t G[x; v_P^\infty t + \Delta m(\boldsymbol{x}_\perp), 2D_e t](\alpha^\infty) = \frac{\exp\left[-\dfrac{v_P^\infty}{2D_e}\left(\sqrt{1 + \dfrac{4D_e \alpha^\infty}{(v_P^\infty)^2}} - 1\right)[x - \Delta m(\boldsymbol{x}_\perp)]\right]}{v_P^\infty \sqrt{1 + 4D_e \alpha^\infty/(v_P^\infty)^2}}.$$
$$(3.25)$$

The requirement $x \geq \Delta m(\boldsymbol{x}_\perp)$ is needed because the Gaussian approximation deteriorates at smaller x. For a given time $t > 0$, the peak of the Gaussian is located at $x = v_P^\infty t + \Delta m$, which implies $x - \Delta m = v_P^\infty t$. This means that under this approximation, the peak at a position $x < \Delta m$ would occur before $t = 0$, resulting in a change of sign of the square root term within the exponential in the Laplace transform. Using (3.25), we conclude that

$$p_s^\infty(\boldsymbol{x}_\perp) = \frac{\beta(\boldsymbol{x}_\perp)\, v_E(\boldsymbol{x}_\perp)\, p_t^\infty(\boldsymbol{x}_\perp)}{\displaystyle\int_{\Omega_\perp} \mathrm{d}\boldsymbol{x}_\perp\, \beta(\boldsymbol{x}_\perp)\, v_E(\boldsymbol{x}_\perp)\, p_t^\infty(\boldsymbol{x}_\perp)}, \quad (3.26a)$$

where

$$\beta(\boldsymbol{x}_\perp) = \exp(\gamma \alpha^\infty \, \Delta m(\boldsymbol{x}_\perp)/\overline{v_E}), \quad \gamma = \frac{2\overline{v_E}}{v_P^\infty} \left[1 + \sqrt{1 + \frac{4\mu_1^2 \overline{v_E}^2}{(v_P^\infty)^2 \, Pe^2}(1 + \eta \, Pe^2)} \right]^{-1}.$$

$$(3.26b,c)$$

Here, we have used the fact that $\mu_1^2 = 2\tau_D \alpha^\infty$ is a constant that depends only on the geometry of the problem and on the Damköhler number, as we will see below. Note that $\gamma \approx Pe/\mu_1$ for $Pe \ll 2\mu_1 \overline{v_E}/v_P^\infty$, $\eta^{-1/2}$, whereas in the opposite limit of large Pe, γ approaches a constant, $\gamma \approx 2\overline{v_E}/v_P^\infty [1 + (1 + 4\mu_1^2 \overline{v_E}^2 \eta/(v_P^\infty)^2)^{1/2}]^{-1} \approx \overline{v_E}/v_P^\infty$. In the last approximation, we have used the fact that the term involving η turns out to be small compared to 1 for both the 2-D and 3-D problems. We note that $\gamma \approx \overline{v_E}/v_P^\infty$ is recovered if the plume is approximated as a Dirac delta rather than a Gaussian along the longitudinal direction. As shown in what follows, the dimensionless quantity $\alpha^\infty \, \Delta m(\boldsymbol{x}_\perp)/\overline{v_E}$ does not depend on the Péclet number, and γ increases monotonically with Pe. The correction factor β is thus largest and, more importantly, most spatially variable as $Pe \to \infty$. Formally, the factor γ is also largest as $\eta \to 0$ for a given Pe, with η depending on Da and geometry, although we find that the value of η has negligible impact for the problems treated here, irrespective of the value of Pe. This means that while the mean plume velocity v_P^∞ is required to estimate γ, a detailed treatment of dispersion is not. For the conservative problem, $\alpha^\infty = 0$, so $\beta(\boldsymbol{x}_\perp) = 1$ and $p_s^\infty = p_{t,F}^\infty$, as expected.

We thus conclude that for the reactive problem, breakthrough is favoured where $\Delta m > 0$, and suppressed where $\Delta m < 0$, in addition to the natural flux-weighting caused by considering advective breakthrough at fixed distance. From the preceding discussion, based on (3.24), we see that this enhancement or suppression of breakthrough is due to the fact that transverse positions where the mean plume position is locally larger are associated with a larger mass at the time of crossing, because solute arrives earlier and is therefore less subject to reaction on average. We find in what follows that the differences between p_s^∞ and $p_{t,F}^\infty$ are non-zero but small for all $Da > 0$ and $Pe > 0$ for the 2-D channel, and are more pronounced for the 3-D channel, even at moderate Da and Pe. In both the 2-D and 3-D cases, the differences between the mean v_t^∞ of the fixed-time transverse velocity p.d.f. and the mean plume velocity v_P^∞, which also result from the same effect, are appreciable starting at moderate Da and Pe. It is interesting to note that as we will see, Δm is non-zero even for the conservative problem, although it no longer plays a role at late times because it does not interact with reaction to create the necessary mass differences.

Finally, we consider the velocity p.d.f. associated with breakthrough over a control plane at a given distance from injection. Analogously to (3.6), we have the relationship

$$p_{v_s}^\infty(v) = |\Omega_\perp| \, p_s^\infty[r_\perp(v)] p_E(v) = |\Omega_\perp| \, p_t^\infty[r_\perp(v)] \frac{\beta[r_\perp(v)] \, \overline{v_E} \, p_F(v)}{\displaystyle\int_0^{v_M} \mathrm{d}v \, \beta[r_\perp(v)] \, v \, p_{v,t}^\infty(v)}. \quad (3.27)$$

Its mean,

$$v_s^\infty = \int_0^{v_M} \mathrm{d}v \, v \, p_{v_s}^\infty(v) = \frac{\displaystyle\int_0^{v_M} \mathrm{d}v \, \beta[r_\perp(v)] \, v^2 \, p_{v_t}^\infty(v)}{\displaystyle\int_0^{v_M} \mathrm{d}v \, \beta[r_\perp(v)] \, v \, p_{v_t}^\infty(v)} = \frac{\displaystyle\int_{\Omega_\perp} \mathrm{d}\boldsymbol{x}_\perp \, \beta(\boldsymbol{x}_\perp) \, v_E^2(\boldsymbol{x}_\perp) \, p_t^\infty(\boldsymbol{x}_\perp)}{\displaystyle\int_{\Omega_\perp} \mathrm{d}\boldsymbol{x}_\perp \, \beta(\boldsymbol{x}_\perp) \, v_E(\boldsymbol{x}_\perp) \, p_t^\infty(\boldsymbol{x}_\perp)},$$

$$(3.28)$$

Symbol	Physical meaning	Fixed	Equations
p_t^∞	Transverse mass p.d.f.	Time	(3.3), (4.3), (4.19)
$p_{t,F}^\infty$	Flux-weighted transverse mass p.d.f.	Time	(3.10), (4.5), (4.21)
p_s^∞	Transverse mass breakthrough p.d.f.	Distance	(3.23a,b), (3.26)
$p_{v_t}^\infty$	Transverse velocity p.d.f.	Time	(3.6), (4.16), (4.27)
$p_{v_t,F}^\infty$	Flux-weighted transverse velocity p.d.f.	Time	(3.9), (4.17), (4.28)
$p_{v_s}^\infty$	Transverse velocity breakthrough p.d.f.	Distance	(3.27)
v_P^∞	Mean plume velocity	Time	(3.13), (4.14), (4.25)
v_t^∞	Mean of transverse velocity p.d.f.	Time	(3.8), (4.13), (4.24)
$v_{t,F}^\infty$	Mean of flux-weighted transverse velocity p.d.f.	Time	(3.11), (4.15), (4.26)
v_s^∞	Mean of transverse breakthrough velocity p.d.f.	Distance	(3.28)

Table 1. Main equilibrium quantities discussed in the text, along with important equations.

represents the mean solute velocity upon crossing a far control plane, i.e. at a longitudinal position far from the initial condition irrespective of the crossing time. Note that for the conservative problem, this velocity p.d.f. is obtained by flux-weighting the fixed-time velocity p.d.f. That is, in that case, $p_{v_s}^\infty(v) = p_{v_t,F}^\infty(v)$ and $v_s^\infty = v_{t,F}^\infty$; see (3.9) and (3.11).

4. Equilibrium distributions

In this section, we determine the transverse equilibrium distributions for surviving mass, breakthrough and velocity introduced in § 3. The main asymptotic quantities discussed in this section are summarized in table 1 for ease of reference. Consider first the conservative problem. The asymptotic concentration field for large times is constant over the cross-section, so that $p_t^\infty(\boldsymbol{x}_\perp) = 1/|\Omega_\perp|$. Thus, in this case, the asymptotic p.d.f. of velocities at fixed time coincides with the Eulerian p.d.f., $p_{v_t}^\infty = p_E$. Since, as already discussed, the correction factor $\beta(\boldsymbol{x}_\perp)$ in (3.26) is unity in this case, breakthrough p.d.f.s are obtained by flux-weighting. Thus we have $p_s^\infty = p_{t,F}^\infty = v_E/(|\Omega_\perp|\,\overline{v_E})$ and $p_{v_s}^\infty = p_{v_t,F}^\infty = p_F$, as expected (Dentz *et al.* 2016).

In what follows, we analyse the reactive problem separately for flow between flat plates (2-D channel) and flow in a cylindrical pipe (3-D channel). We compare our results to numerical simulations obtained using a standard finite-volume method in OpenFOAM (OpenCFD Ltd 2022). For the simulations, we fix a moderate Péclet number $Pe = 2$, and consider three values of the Damköhler number, $Da = 10^{-1}$, 1 and 10, corresponding to slow, moderate and fast reaction compared to diffusion at the scale of the channel radius (see Appendix C for further details).

4.1. *Two-dimensional channel*

In this case, the diffusion equation (2.6) with boundary conditions (2.7) and initial condition $c_\perp(y; 0)$ has the solution (Polyanin & Nazaikinskii 2016)

$$c_\perp(y; t) = \sum_{n \geq 1} \exp\left(-\frac{\mu_n^2 t}{2\tau_D}\right) \frac{\phi_n(y)}{ab_n} \int_{-a}^{a} \mathrm{d}y'\, \phi_n(y')\, c_\perp(y'; 0), \qquad (4.1a)$$
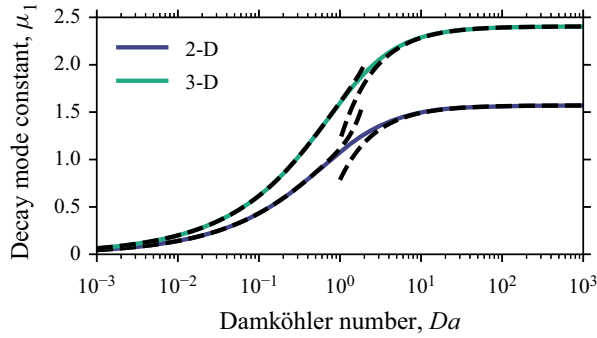
Figure 1. Slowest decay mode constant μ_1 as a function of *Da* for the 2-D and 3-D channels. The solid lines are obtained by finding the smallest solution to (4.1*d*) and (4.18*b*) numerically. The analytical limiting forms (E1) and (F1) for small *Da*, and (E2) and (F2) for large *Da*, are shown as dashed lines for $Da \leq 1$ and $Da \geq 1$, respectively.

where

$$\phi_n(y) = \cos\left[\mu_n\left(1 + \frac{y}{a}\right)\right] + \frac{2\,Da}{\mu_n}\sin\left[\mu_n\left(1 + \frac{y}{a}\right)\right], \tag{4.1b}$$

$$b_n = 1 + \frac{2\,Da\,(1 + 2\,Da)}{\mu_n^2}, \tag{4.1c}$$

and μ_n are the positive solutions to

$$\frac{\tan(2\mu)}{2\mu} = \frac{2\,Da}{\mu^2 - (2\,Da)^2}. \tag{4.1d}$$

Trigonometric manipulation yields two useful alternate forms of this relation:

$$\cos(2\mu) = \frac{\mu^2 - (2\,Da)^2}{\mu^2 + (2\,Da)^2}, \quad \tan(\mu) = \frac{2\,Da}{\mu}. \tag{4.1e}$$

The μ_n dictate the rate of decay of mode n in (4.1*a*) through the exponential factor. While they cannot in general be determined analytically, by ordering the solutions so that $\mu_n < \mu_{n+1}$, it holds that the $n = 1$ mode is dominant for $t \gtrsim 2\tau_D/(\mu_2^2 - \mu_1^2)$, so that for large times,

$$c_\perp(y; t) \approx \exp\left(-\frac{\mu_1^2 t}{2\tau_D}\right)\frac{\phi_1(y)}{ab_1}\int_{-a}^{a} \mathrm{d}y'\,\phi_1(y')\,c_\perp(y'; 0). \tag{4.2}$$

The dependency of μ_1 on *Da* is shown in figure 1, along with the 3-D case discussed in § 4.2 for comparison. Analytical results for the low and high Damköhler limits are derived in § E.1.

The onset of the asymptotic regime depends only weakly on the reaction time τ_R, through the dependence of the decay mode constants μ_n on the Damköhler number. Indeed, $\mu_2^2 - \mu_1^2$ grows monotonically from ≈ 10 to ≈ 20 for the 2-D case, so that the characteristic time for the onset of the asymptotic regime decreases with *Da* but is always of the order of a tenth of the diffusion time. It may seem surprising that the time τ_R does not enter more directly, but this can be understood as follows. In the high-*Da* limit, the reaction is transport-limited, so that the transition to the asymptotic regime is

985 A16-12

controlled by diffusion. On the other hand, in the low *Da* limit, the equilibrium profile is close to homogeneous, so that little reaction is necessary to achieve it, and the diffusive homogenization time remains the most important control. Similar considerations are valid for the 3-D case, for which $\mu_2^2 - \mu_1^2$ grows monotonically from ≈ 15 to ≈ 25.

4.1.1. *Surviving mass and breakthrough*

From (3.2) and (4.2), we obtain the equilibrium surviving mass p.d.f.

$$
p_t^\infty(y) = \frac{\phi_1(y)}{\displaystyle\int_{-a}^{a} dy'\, \phi_1(y')} = \frac{\mu_1^2}{4a\,Da}\left(\cos\left[\mu_1\left(1+\frac{y}{a}\right)\right] + \frac{2\,Da}{\mu_1}\sin\left[\mu_1\left(1+\frac{y}{a}\right)\right]\right),
$$
(4.3)

where we have used (4.1*e*) and some trigonometric manipulation.

We conclude that for arbitrary reaction rate and including $Da \to \infty$, the transverse distribution of surviving mass admits an asymptotic form that is independent of the initial condition. From (4.1*a*), we also conclude immediately that the late-time reaction rate is constant and given by the slowest decay mode,

$$
\alpha^\infty = \frac{\mu_1^2}{2\tau_D}.
$$
(4.4)

This result can be verified to agree with (3.14) by direct calculation using (4.3) and the trigonometric relations (4.1*e*). The fact that the asymptotic rate is constant is consistent with the existence of a transverse equilibrium distribution. The relationship to recent descriptions in terms of first passage times (Aquino & Le Borgne 2021*a*; Aquino *et al.* 2023) is discussed in Appendix D.

To obtain the flux-weighted surviving mass p.d.f. $p_{t,F}^\infty$, we flux-weight (4.3) according to (3.10):

$$
p_{t,F}^\infty(y) = \frac{Da\,\mu_1^2}{2\,Da - \mu_1^2}\left(1 - \frac{y^2}{a^2}\right)p_t^\infty(y);
$$
(4.5)

see also (4.13) below for the mean of the fixed-time velocity p.d.f. The limiting forms of p_t^∞ and $p_{t,F}^\infty$ for small and large *Da* are derived in § E.1.

To obtain the true breakthrough p.d.f. p_s^∞ associated with flux over a fixed control plane, we must take into account the correction factor $\beta(y) = \exp[\gamma\alpha^\infty\,\Delta m(y)/\overline{v_E}]$; see (3.26). Because of the normalization, any differences between p_s^∞ and $p_{t,F}^\infty$ result from variability in the mean-position discrepancy $\Delta m(y)$ with respect to the cross-section position *y*. To compute it, we must solve (3.20) for the auxiliary quantity $f(y, t)$. Since the differential operators are the same as for the transverse ADE (2.6), this equation has the same propagator, except that the decay modes are modified by the production term at rate α^∞. The solution for the 2-D channel, reflecting the presence of a source term $p_t^\infty(y)v_E(y)$, is (Polyanin & Nazaikinskii 2016)

$$
f(y, t) = \sum_{n \geq 1}\frac{\phi_n(y)}{ab_n}\left[\exp\left(-\left(\frac{\mu_n^2}{2\tau_D} - \alpha^\infty\right)t\right)\int_{-a}^{a}dy'\,\phi_n(y')f(y', 0)\right.
$$
(4.6)

$$
\left. + \int_0^t dt'\exp\left(-\left(\frac{\mu_n^2}{2\tau_D} - \alpha^\infty\right)t'\right)\int_{-a}^{a}dy'\,p_t^\infty(y')\,\phi_n(y')\,v_E(y')\right],
$$
(4.7)

where the ϕ_n and μ_n are the same as in (4.1a). We assume that the initial condition $f(y,0) \propto \int dx\, x\, c(x,y,0)$ does not depend on y, which holds for any initial condition of constant width along the longitudinal direction. We then set $f(y,0) = 0$ without further loss of generality by choosing the longitudinal origin of the coordinate system to coincide with the initial mean plume position. Using (4.3) and (4.4), we obtain, for $t \gg 2\tau_D/(\mu_2^2 - \mu_1^2)$,

$$f(y,t) = \frac{16a\, Da^2\, t\, p_t^\infty(y)}{\mu_1^4 b_1} \int_{-a}^{a} dy'\, (p_t^\infty)^2(y')\, v_E(y') \tag{4.8}$$

$$+ \sum_{n \geq 2} \frac{\phi_n(y)}{ab_n \alpha^\infty} \frac{\mu_1^2}{\mu_n^2 - \mu_1^2} \int_{-a}^{a} dy'\, p_t^\infty(y')\, \phi_n(y')\, v_E(y'). \tag{4.9}$$

The first term is associated with the mean plume velocity as discussed below. From the second term and (3.19a,b) and (3.21), we conclude that the late-time mean-position discrepancy obeys

$$\frac{\alpha^\infty}{\overline{v_E}} \Delta m(y) = -\frac{3}{2p_t^\infty(y)} \sum_{n \geq 2} \frac{\phi_n(y)}{b_n} \frac{\mu_1^2}{\mu_n^2 - \mu_1^2} \int_{-1}^{1} du\, u^2\, p_t^\infty(au)\, \phi_n(au), \tag{4.10}$$

where we have used the fact that $p_t^\infty(y) \propto \phi_1(y)$ and the ϕ_n are a set of orthogonal modes (i.e. the product $\phi_n \phi_m$ integrates to zero for $n \neq m$). We note that for an initial condition where $f(y,0)$ is not constant, there is an additional contribution to $\Delta m(y)$ given by $\phi_1(y)/(ab_1) \int dy'\, \phi_1(y') f(y',0)$, which cannot be fully removed by a choice of coordinate origin. We are not aware of a closed-form solution of (4.10) for arbitrary Da. However, rather surprisingly, the remaining integration and sum can both be performed analytically in the limit of large Da to yield the simple form

$$\frac{\alpha^\infty}{\overline{v_E}} \Delta m(y) = \frac{1}{8} \left[\frac{3y^2}{a^2} - \frac{\pi y}{a} \left(1 - \frac{y^2}{a^2} \right) \tan\left(\frac{\pi y}{2a} \right) + \frac{12}{\pi^2} - 1 \right]. \tag{4.11}$$

Unfortunately, the denominator in (3.26) must still be computed numerically. As mentioned in § 3.3, Δm is non-zero even for the reactive problem. In that case, proceeding similarly using the conservative solution (Polyanin & Nazaikinskii 2016), we obtain

$$\frac{\Delta m(y)}{2\tau_D \overline{v_E}} = \frac{1}{8} \left[\frac{7}{30} - \frac{y^2}{a^2} \left(1 - \frac{y^2}{2a^2} \right) \right]. \tag{4.12}$$

We find by numerical computation according to (4.10), using the values of μ_n up to $n = 6$ reported in Carslaw & Jaeger (1986), that this result is approached continuously in the limit of small Da.

Figure 2(a) illustrates the dependency of the factor γ on Péclet number (see (3.26)), and figure 2(b) shows a comparison between p_s^∞ and $p_{t,F}^\infty$ at large Da and Pe, showing little difference. The value of η in γ depends on the Damköhler number, as discussed in relation to (2.9) for Taylor dispersion. However, this dependency makes no appreciable difference in either two or three dimensions for the quantities reported here, and we employ $\eta = 0$ in (3.26b) here and in what follows. The largest error in γ occurs for $Pe \to \infty$ and $Da \to \infty$, with a relative value of about 4×10^{-3} in two dimensions, and 2×10^{-4} in three dimensions. The error decreases to zero as $Da \to 0$. The results for the p.d.f.s
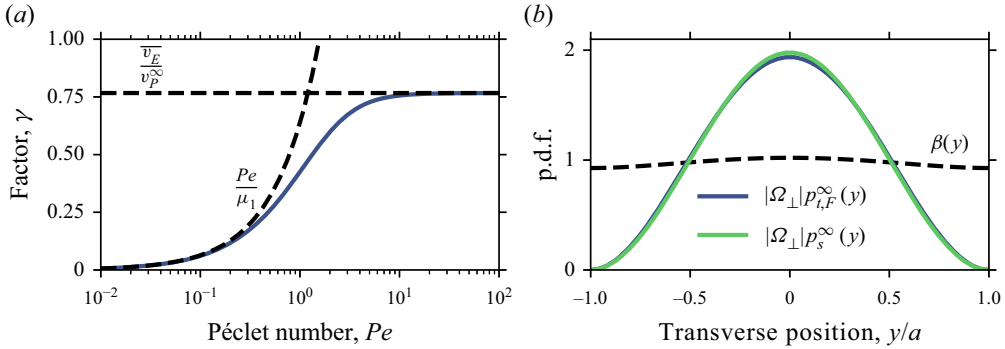
Figure 2. Effect of the mean-position discrepancy $\Delta m(y)$ on the breakthrough p.d.f. p_s^∞ for the 2-D channel. The mean-position discrepancy generates differences between the flux-weighted p.d.f. $p_{t,F}^\infty$ and the true breakthrough p.d.f. p_s^∞ through the factor $\beta(y) = \exp[-\gamma\alpha^\infty \Delta m(y)/\overline{v_E}]$ in (3.26). (*a*) Plot of γ as a function of Péclet number Pe in the limit of infinite Da, with the low- and high-Pe behaviours shown as dashed lines. (*b*) Comparison of p_s^∞ ((3.26) and (4.10)) and $p_{t,F}^\infty$ (E6) in the limit of large Da and Pe, showing that differences are minor for the 2-D channel; the factor $\beta(y)$, which is below 1 near the channel walls and above 1 near the channel centre but always close to unity, is shown as a dashed line.
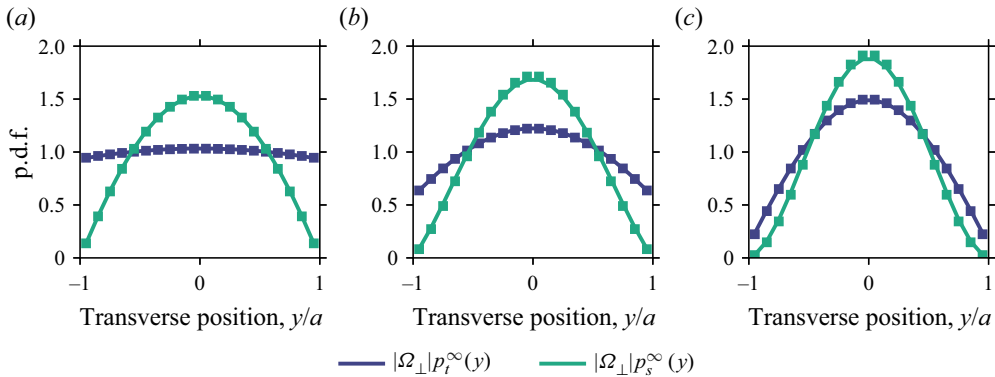
Figure 3. Equilibrium surviving mass and breakthrough p.d.f.s p_t^∞ and p_s^∞ in the 2-D channel, for (*a*) $Da = 10^{-1}$, (*b*) $Da = 1$, and (*c*) $Da = 10$. Symbols show the results of numerical simulations. The theoretical predictions approximate the breakthrough p.d.f. p_s^∞ as the flux-weighted p.d.f. $p_{t,F}^\infty$ as discussed in the text. The solid lines in (*a,c*) show the analytical limit forms (E3) and (E5) for low Da, and (E4) and (E6) for high Da, respectively. The solid lines in (*b*) show the analytical solutions (4.3) and (4.5) with μ_1 computed numerically according to (4.1*d*).

under the approximation $p_s^\infty \approx p_{t,F}^\infty$ are shown in figure 3 for different Da and $Pe = 2$. As expected, since the effect of β is small at large Da and Pe, the agreement is good across all values of Da.

4.1.2. *Velocity*

Using (2.2), (3.8) and (4.3), we determine the asymptotic mean of the fixed-time velocity p.d.f. as

$$\frac{v_t^\infty}{\overline{v_E}} = 3\frac{1 - \mu_1 \cot \mu_1}{\mu_1^2} = \frac{3}{2}\frac{2\,Da - \mu_1^2}{Da\,\mu_1^2}. \tag{4.13}$$
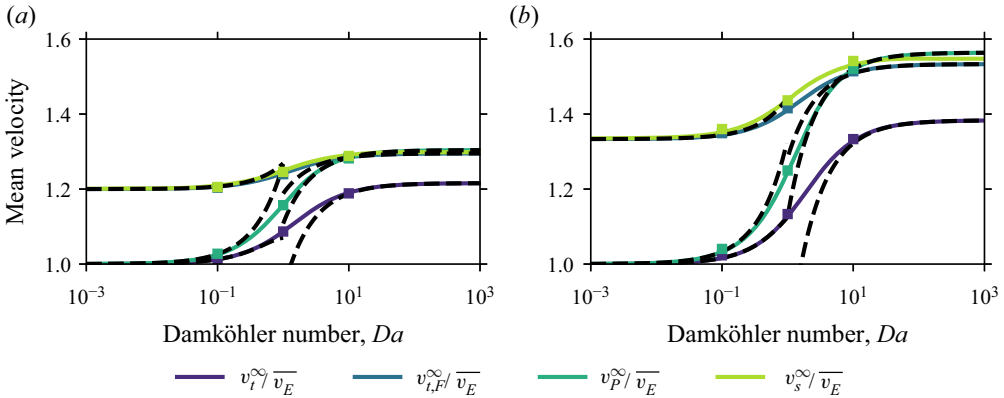
Figure 4. Equilibrium mean of the transverse velocity p.d.f. in time v_t^∞, its flux-weighted counterpart $v_{t,F}^\infty$, mean plume velocity v_P^∞, and mean breakthrough velocity v_s^∞, as a function of Da for (*a*) the 2-D channel and (*b*) the 3-D channel. The solid lines corresponding to v_t^∞, v_P^∞ and $v_{t,F}^\infty$ are the analytical solutions (*a*) (4.13), (4.14) and (4.15), and (*b*) (4.24), (4.25) and (4.26). The corresponding dashed lines show the analytical limit forms for low and high Da: (*a*) (E7), (E9) and (E11), and (E8), (E10) and (E12); (*b*) (F7), (F9) and (F11), and (F8), (F10) and (F12). Solid lines corresponding to v_s^∞ employ (3.28), together with (4.10) for (*a*) and (4.23) for (*b*); these lines use Péclet number $Pe \to \infty$. Symbols show the results of numerical simulations for $Da = 10^{-1}$, 1 and 10.

As discussed in § 3.2, this is smaller than the mean plume velocity v_P^∞, which describes the rate of change of the plume centre of mass at late times. We find from (3.17) and (4.8) that

$$\frac{v_P^\infty}{\overline{v_E}} = \frac{16\,Da^2}{\mu_1^4 b_1} \int_{-1}^{1} \mathrm{d}u\, u^2\,(p_t^\infty)^2(u) = 1 + \frac{3}{4\mu_1^2} - \frac{3 + 4\,Da}{2\mu_1^2 + 4\,Da\,(1 + 2\,Da)}. \quad (4.14)$$

This result is equivalent to that reported in Lungu & Moffatt (1982). Using (4.3) for p_t^∞, (4.11) for $\alpha_\infty\,\Delta m(y)/\overline{v_E}$, (4.13) and (4.14) for $v_t^\infty/\overline{v_E}$ and $v_P^\infty/\overline{v_E}$, and $\Delta m_W = \Delta m(\pm a)$, we find by direct calculation that (3.22) is satisfied as expected.

In line with the discussion for the breakthrough p.d.f., we approximate the true average breakthrough velocity v_s^∞ by the flux-weighted mean $v_{t,F}^\infty$. Proceeding similarly to the calculation of v_t^∞, using (3.11), we obtain

$$\frac{v_{t,F}^\infty}{\overline{v_F}} = \frac{15}{\mu_1^2}\left(1 - \frac{\overline{v_E}}{v_t^\infty}\right). \quad (4.15)$$

These results are shown as a function of Da in figure 4(*a*) (see § E.2 for the derivation of the high- and low-Da forms). The 3-D case, discussed in detail in § 4.2, is shown in figure 4(*b*) for comparison.

It is interesting to note that for both the 2-D and 3-D channels, we have $\overline{v_E} < \overline{v_F} < v_t^\infty < v_{t,F}^\infty < v_s^\infty < v_P^\infty$ as $Da \to \infty$. In this high-Da limit, there is a noticeable difference corresponding to an increase of approximately 7 % and 13 % between v_t^∞ and v_P^∞ in two and three dimensions, respectively. The plume velocity v_P^∞ differs from the fixed-time flux-weighted velocity $v_{t,F}^\infty$ by only approximately 1 % and 2 %, respectively, and the fixed-time average velocity v_t^∞ is similar to the Eulerian flux-weighted mean velocity $\overline{v_F}$ rather than to the Eulerian mean velocity $\overline{v_E}$, differing by about 1 % in the 2-D case, and 4 % in the 3-D case. The average breakthrough velocity v_s^∞ is approximately halfway

between v_P^∞ and $v_{t,F}^\infty$ in both cases. This should be contrasted with the conservative problem, for which $v_t^\infty = v_P^\infty = \overline{v_E}$ and $v_s^\infty = v_{t,F}^\infty = \overline{v_F}$. As shown in table 2, $\overline{v_F}$ is larger than the mean flow velocity $\overline{v_E}$ by 20 % and approximately 33 % in two and three dimensions; thus the mean plume velocity increases by approximately 30 % and 56 % as $Da \to \infty$.

It is easy to see that the relationship $\overline{v_E} \leq \overline{v_F}$ always holds, with the equality holding if and only if the flow is uniform, due to fact that $\overline{v_F}$ assigns more weight to higher velocities. The same argument shows that $v_t^\infty \leq v_{t,F}^\infty$, and similarly, because breakthrough at fixed distance is naturally associated with a flux-weighting according to the local velocities, $v_t^\infty \leq v_s^\infty$. Since reaction happens at the channel walls, it leads to an increase of the velocities sampled by the plume, and therefore to an increase in the different Lagrangian (i.e. associated with sampling by the solute rather than characteristic of the flow) average velocities v_t^∞, $v_{t,F}^\infty$, v_s^∞ and v_P^∞. Thus it is also easy to see that for the reactive problem, $\overline{v_E} < v_t^\infty, v_P^\infty$ and $\overline{v_F} < v_{t,F}^\infty, v_s^\infty$. We have seen that the inequality $v_{t,F}^\infty < v_s^\infty$ of two averages that are identical for the conservative problem arises from the interaction between the subleading moment discrepancy Δm and reaction. Indeed, breakthrough is favoured where $\Delta m > 0$, because the earlier arrival of Lagrangian trajectories at these positions means a shorter exposure to reaction; see (3.26). Given that $\Delta m \neq 0$, it is intuitive that the mean plume position for a given transverse position is larger where the flow velocity is larger. This mechanism acts in addition to the natural flux-weighting associated with breakthrough, and leads to $v_{t,F}^\infty < v_s^\infty$. For a similar reason, $v_t^\infty < v_P^\infty$; see (3.15). It should be noted that these qualitative arguments are not sufficient to ensure that for sufficiently fast reaction, the fixed-time averages v_P^∞ and v_t^∞ become larger than the flux-weighted Eulerian average $\overline{v_F}$, and similarly that v_P^∞ becomes larger than both the Lagrangian flux-weighted average $v_{t,F}^\infty$ and the breakthrough average v_s^∞, as we observe in figure 4. In other words, this discussion does not guarantee that this happens at finite Da for an arbitrary flow configuration.

We also note in this context that the inequality of Lagrangian and Eulerian average velocities is not limited to the reactive problem when considering early times. For the conservative problem, the classical Taylor dispersion picture implies that the asymptotic fixed-time transverse average velocity and the plume velocity both equal the average flow velocity $\overline{v_E}$, and similarly the average flux-weighted and breakthrough velocities equal $\overline{v_F}$. However, this is not true at pre-asymptotic times, when these quantities may differ as the initial plume deforms as it samples the flow, and complex pre-asymptotic distributions of transverse concentration and breakthrough may develop (Guan & Chen 2024).

Next, we turn to the asymptotic velocity p.d.f.s. For the fixed-time p.d.f., using (3.6), (3.7) and (4.3), we obtain

$$\frac{p_{v_t}^\infty(v)}{p_E(v)} = \frac{\mu_1^2}{2\,Da} \left(\cos\left[\mu_1\left(1 + \sqrt{1 - \frac{v}{v_M}}\right)\right] + \frac{2\,Da}{\mu_1} \sin\left[\mu_1\left(1 + \sqrt{1 - \frac{v}{v_M}}\right)\right] \right). \tag{4.16}$$

Recall that the maximum velocity is $v_M = 3\overline{v_E}/2$ for two dimensions. For $v \ll v_M$, we find by Taylor expansion that the low-velocity behaviour is flat, as for the conservative case. However, as $Da \to \infty$ and $\mu_1 \to \pi/2$, the v-independent term vanishes. The low-velocity plateau, which accounts for contributions from the shear layer near the channel walls, is thus lower for higher Da, and occurs for smaller v. The approach to this plateau is $\sim v$, and the scaling of the p.d.f. thus becomes linear in v as $Da \to \infty$. For $v \approx v_M$, corresponding to positions near the centre of the channel, we have $p_{v_t}^\infty(v) \sim 1/\sqrt{v - v_M}$
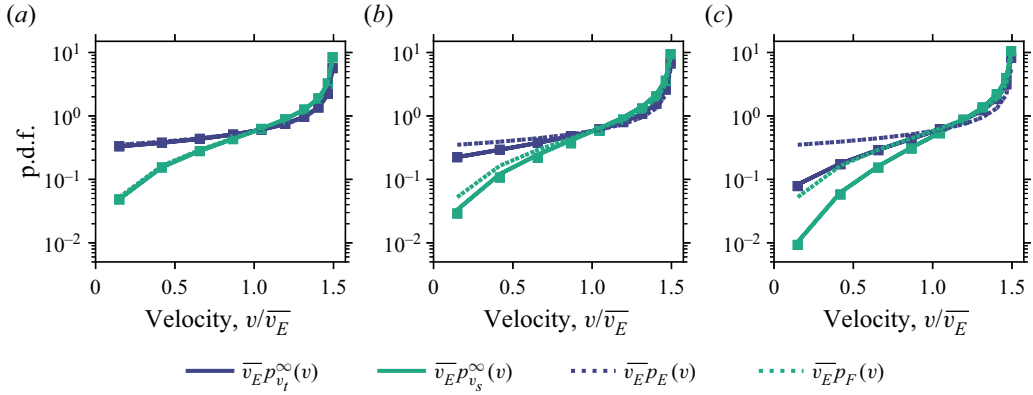
Figure 5. Equilibrium velocity p.d.f. in time $p_{v_t}^\infty$ and breakthrough velocity p.d.f. $p_{v_s}^\infty$ in the 2-D channel, for (a) $Da = 10^{-1}$, (b) $Da = 1$, and (c) $Da = 10$. Symbols show the results of numerical simulations. The theoretical predictions approximate $p_{v_s}^\infty$ as the flux-weighted p.d.f. $p_{v_t,F}^\infty$ as discussed in the text. The solid lines in (a,c) show the analytical limit forms (E13) and (E15) for low Da, and (E14) and (E16) for high Da, respectively. The solid lines in (b) show the analytical solutions (4.16) and (4.17), with μ_1 computed numerically according to (4.1d). Dotted lines show the Eulerian and flux-weighted Eulerian velocity p.d.f.s $p_E(v)$ and $p_F(v)$, which equal $p_{v_t}^\infty$ and $p_{v_s}^\infty = p_{v_t,F}^\infty$ for the conservative problem.

as for the conservative case, irrespective of Da (see § E.2 for further details on the low- and high-Da limits).

In line with the results for the breakthrough p.d.f., we approximate the true velocity p.d.f. $p_{v_s}^\infty$ associated with breakthrough at fixed distance by the flux-weighted p.d.f. $p_{v_t,F}^\infty$. Flux-weighting (4.16) and using (4.13), we find

$$
\frac{p_{v_t,F}^\infty(v)}{p_F(v)} = \frac{\mu_1^4}{6\,Da - 3\mu_1^2}\left(\cos\left[\mu_1\left(1+\sqrt{1-\frac{v}{v_M}}\right)\right] + \frac{2\,Da}{\mu_1}\sin\left[\mu_1\left(1+\sqrt{1-\frac{v}{v_M}}\right)\right]\right).
$$
(4.17)

The low-velocity scaling is now linear for finite Da, and becomes quadratic as $Da \to \infty$. As before, for high velocities $v \approx v_M$, the scaling is $p_{v_t,F}^\infty(v) \sim 1/\sqrt{v - v_M}$, irrespective of Da. The flux-weighted approximation agrees well with numerical simulations, as can be seen in figure 5.

4.2. *Three-dimensional channel*

Similarly to the 2-D case, decay modes of order higher than the first can be neglected at late times for transport in a cylindrical channel. Furthermore, in this case, symmetry ensures that any angular variability in the initial concentration along the channel cross-section vanishes at late times. The late-time solution for transverse concentrations is thus associated with the slowest radial decay mode and is given by (Polyanin & Nazaikinskii 2016)

$$
c_\perp(\boldsymbol{x}_\perp, t) = \frac{2}{a^2\,\mathrm{J}_1^2(\mu_1)}\frac{(2\,Da)^2}{\mu_1^2 + (2\,Da)^2}\exp\left(\frac{-\mu_1^2 t}{2\tau_D}\right)\mathrm{J}_0\left(\mu_1\frac{|\boldsymbol{x}_\perp|}{a}\right)
$$
$$
\times \int_0^a \mathrm{d}r\, r\,\mathrm{J}_0\left(\mu_1\frac{r}{a}\right)c_\perp(r, 0),
$$
(4.18a)

where J_ν is the Bessel function of the first kind of order ν, and μ_1 is the smallest positive root of

$$\mu\, J_1(\mu) = 2\,Da\, J_0(\mu). \tag{4.18b}$$

Using the well-known recurrence relation $2\alpha\, J_\alpha(x)/x = J_{\alpha-1}(x) + J_{\alpha+1}(x)$ (Abramowitz & Stegun 1964) for $\alpha = 1, 2$, we find that the latter is equivalent to

$$J_2(\mu) = \frac{4\,Da - \mu^2}{\mu^2}\, J_0(\mu), \quad J_3(\mu) = 2\,\frac{8\,Da - 2\mu^2 - Da\,\mu^2}{\mu^3}\, J_0(\mu). \tag{4.18c,d}$$

The behaviour of μ_1 as a function of Da is shown in figure 1(b); see § F.1 for the derivation of the asymptotic forms. Note that the nth radial mode decays exponentially at rate $\mu_n^2/(2\tau_D)$ as for the 2-D case, although the values of μ_n are different because they now solve (4.18b).

4.2.1. *Surviving mass and breakthrough*

From (4.18a), we obtain the surviving mass p.d.f.

$$p_t^\infty(\boldsymbol{x}_\perp) = \frac{\mu_1}{2\pi a^2}\, \frac{J_0(\mu_1 |\boldsymbol{x}_\perp|/a)}{J_1(\mu_1)}. \tag{4.19}$$

Again, we conclude in particular that an equilibrium form independent of the initial condition exists for all Da, including $Da \to \infty$. As before, the asymptotic reaction rate is given by

$$\alpha^\infty = \frac{\mu_1^2}{2\tau_D}. \tag{4.20}$$

Flux-weighting, we find

$$p_{t,F}^\infty(\boldsymbol{x}_\perp) = \frac{Da\,\mu_1^2}{4\,Da - \mu_1^2}\left(1 - \frac{|\boldsymbol{x}_\perp|^2}{a^2}\right) p_t^\infty(\boldsymbol{x}_\perp); \tag{4.21}$$

see also the result for the fixed-time average velocity in (4.24) below. The limiting forms of these two p.d.f.s for $Da \to 0$ and $Da \to \infty$ are discussed in § F.1.

To find the breakthrough p.d.f. p_s^∞, we must solve (3.20). As for the 2-D case, we assume that the initial condition $f(\boldsymbol{x}_\perp, 0) \propto \int \mathrm{d}x\, x\, c(x, \boldsymbol{x}_\perp, 0)$ does not depend on $\boldsymbol{x}_\perp$, and we set $f(\boldsymbol{x}_\perp, 0) = 0$ without further loss of generality. Analogously to the 2-D channel, the solution for $t \gg 2\tau_D/(\mu_2^2 - \mu_1^2)$ is now (Polyanin & Nazaikinskii 2016)

$$
\begin{aligned}
f(\boldsymbol{x}_\perp, t) &= \frac{8\pi^2 a^2 \mu_1^{-2} t\, p_t^\infty(\boldsymbol{x}_\perp)}{1 + (\mu_1/2\,Da)^2} \int_0^a \mathrm{d}r\, r (p_t^\infty)^2(r)\, v_E(r) \\
&+ \frac{2}{a^2 \alpha^\infty} \sum_{n\geq 2} \frac{J_1^{-2}(\mu_n)\, J_0(\mu_n |\boldsymbol{x}_\perp|/a)}{1 + (\mu_n/2\,Da)^2}\, \frac{\mu_1^2}{\mu_n^2 - \mu_1^2} \int_0^a \mathrm{d}r\, r\, p_t^\infty(r)\, J_0(\mu_n r/a)\, v_E(r).
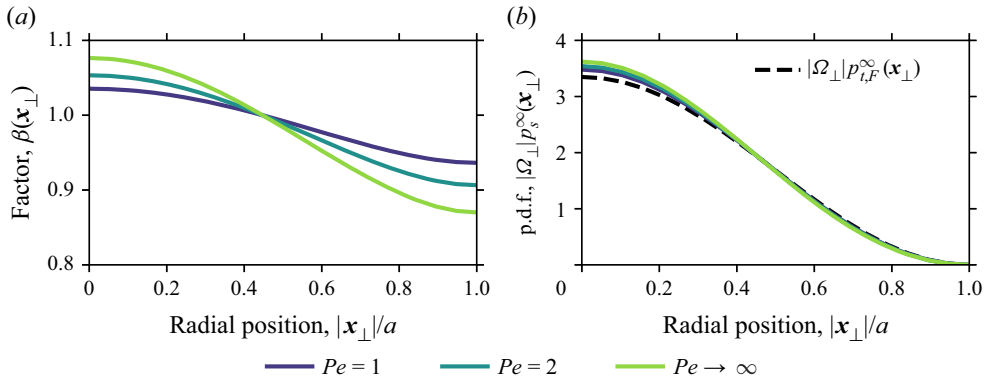\end{aligned}
\tag{4.22}
$$

Figure 6. Effect of the mean-position discrepancy $\Delta m(\boldsymbol{x}_\perp)$ on the breakthrough p.d.f. p_s^∞ for the 3-D channel. The mean-position discrepancy generates differences between the flux-weighted p.d.f. $p_{t,F}^\infty$ and the true breakthrough p.d.f. p_s^∞ through the factor $\beta(\boldsymbol{x}_\perp)$ in (3.26). (a) Behaviour of β in the limit of infinite Da, for different values of Péclet number Pe. (b) Comparison of the resulting p_s^∞ ((3.26) and (4.23), using terms up to $n = 6$ in the sum according to the values of μ_n reported in Carslaw & Jaeger 1986) to $p_{t,F}^\infty$ (F6).

As before, the first term is associated with the mean plume velocity (see below), and from (3.19a,b) and (3.21) we conclude from the second term that

$$\frac{\alpha^\infty}{v_E} \, \Delta m(\boldsymbol{x}_\perp) = -4 \sum_{n \geq 2} \frac{\mathrm{J}_0(\mu_n \, |\boldsymbol{x}_\perp|/a)}{\mathrm{J}_1^2(\mu_n) \, \mathrm{J}_0(\mu_1 \, |\boldsymbol{x}_\perp|/a)} \, \frac{(2 \, Da)^2}{(2 \, Da)^2 + \mu_n^2} \, \frac{\mu_1^2}{\mu_n^2 - \mu_1^2}$$
$$\times \int_0^1 \mathrm{d}u \, u^3 \, \mathrm{J}_0(\mu_1 u) \, \mathrm{J}_0(\mu_n u). \tag{4.23}$$

We are not aware of a closed-form solution for either the integral or the sum in this case.

Recall that the mean-position discrepancy affects the breakthrough p.d.f. p_s^∞ through the factor $\beta(\boldsymbol{x}_\perp)$ in (3.26). The β profiles for different values of the Péclet number at infinite Da are shown in figure 6(a), along with a comparison between the resulting p_s^∞ and the flux-weighted p.d.f. $p_{t,F}^\infty$ in figure 6(b). Although the difference to the flux-weighted p.d.f. is not dramatic, it is substantially more pronounced than in the 2-D case, and clearly discernible at the channel centre. At $Pe = 2$, the results are similar to those for $Pe \to \infty$, which explains the good agreement found between simulations at $Pe = 2$ and theory for $Pe \to \infty$ for the mean breakthrough velocity in figure 4(b). The results for the surviving mass and breakthrough p.d.f.s are shown in figure 7 for different Da at $Pe = 2$. As expected, the differences between p_s^∞ and $p_{t,F}^\infty$ become more pronounced with increasing Da, but are already visible at $Da = 10^{-1}$.

4.2.2. *Velocity*

Proceeding as for the 2-D case, but integrating (3.8) in polar coordinates and consulting table 2 for the 3-D case, we obtain for the asymptotic mean of the fixed-time velocity p.d.f.:

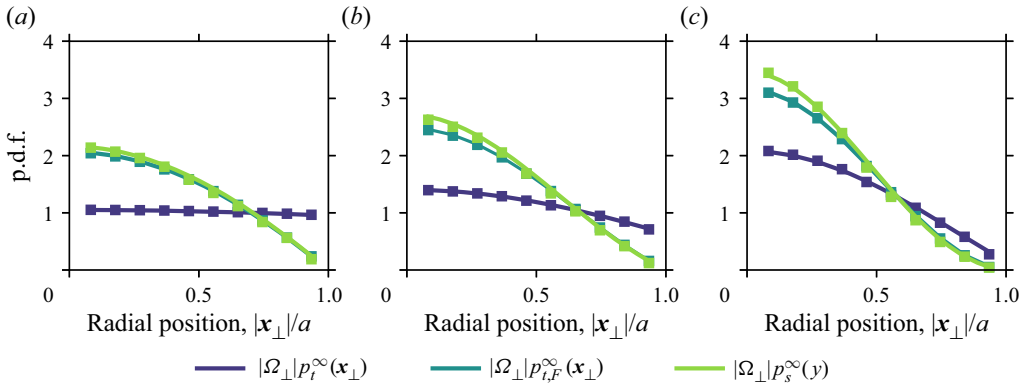$$\frac{v_t^\infty}{v_E} = 2 \, \frac{4 \, Da - \mu_1^2}{Da \, \mu_1^2}. \tag{4.24}$$

Figure 7. Equilibrium surviving mass and breakthrough p.d.f.s p_t^∞ and p_s^∞, and flux-weighted mass p.d.f. $p_{t,F}^\infty$, in the 3-D channel, for (*a*) $Da = 10^{-1}$, (*b*) $Da = 1$, and (*c*) $Da = 10$. Symbols show the results of numerical simulations. The solid lines in (*a,c*) for p_t^∞ and $p_{t,F}^\infty$ show the analytical limiting forms (F3) and (F5) for low *Da*, and (F4) and (F6) for high *Da*. The corresponding solid lines in (*b*) show the analytical solutions (4.19) and (4.21), with μ_1 computed numerically according to (4.18*b*). In all plots, the solid lines representing p_s^∞ are computed using (3.26) and (4.23), using terms up to $n = 6$ in the sum according to the values of μ_n reported in Carslaw & Jaeger (1986).

Using (4.22), arguments similar to those for the 2-D case lead to the asymptotic plume velocity

$$\frac{v_P^\infty}{\overline{v_E}} = \frac{8\pi^2}{\mu_1^2} \frac{(2\,Da)^2}{\mu_1^2 + (2\,Da)^2} \int_0^a \mathrm{d}r\, r\, (p_t^\infty)^2(r)\, v_E(r) = \frac{4}{3}\left(1 + \frac{1}{\mu_1^2} - \frac{1 + 2\,Da}{\mu_1^2 + (2\,Da)^2}\right), \tag{4.25}$$

This result is equivalent to that reported in Lungu & Moffatt (1982). For the flux-weighted mean velocity, we find

$$\frac{v_{t,F}^\infty}{\overline{v_F}} = \frac{24}{\mu_1^2}\left(1 - \frac{\overline{v_E}}{v_t^\infty}\right). \tag{4.26}$$

The different mean velocities are shown as a function of *Da* in figure 4(*b*); see also the associated discussion in §§ 4.1.2 and F.2 for the limiting forms at low and high *Da*.

We now turn to the asymptotic velocity p.d.f.s, again proceeding as for the one-dimensional case. First, according to (3.6), the fixed-time p.d.f. is given by

$$\frac{p_{v_t}^\infty(v)}{p_E(v)} = \frac{\mu_1}{2\pi a^2\, \mathrm{J}_1(\mu_1)}\, \mathrm{J}_0\left(\mu_1\sqrt{1 - \frac{v}{v_M}}\right). \tag{4.27}$$

Note that in this case, the Eulerian p.d.f. $p_E(v) = 1/v_M$ is independent of v; see table 2. Finally, for the flux-weighted p.d.f., we have

$$\frac{p_{v_t,F}^\infty(v)}{p_F(v)} = \frac{\mu_1^3}{4\pi a^2\, \mathrm{J}_1(\mu_1)}\, \frac{Da}{4\,Da - \mu_1^2}\, \mathrm{J}_0\left(\mu_1\sqrt{1 - \frac{v}{v_M}}\right). \tag{4.28}$$

These velocity p.d.f.s are illustrated in figure 8 (see § F.2 for low- and high-*Da* forms) along with the breakthrough velocity p.d.f. $p_{v_s}^\infty$ from (3.27) that takes into account the mean-position discrepancy (4.23). The differences between $p_{v_s}^\infty$ and $p_{v_t,F}^\infty$ are in line with the discussion of the breakthrough p.d.f. p_s^∞; see figure 7.
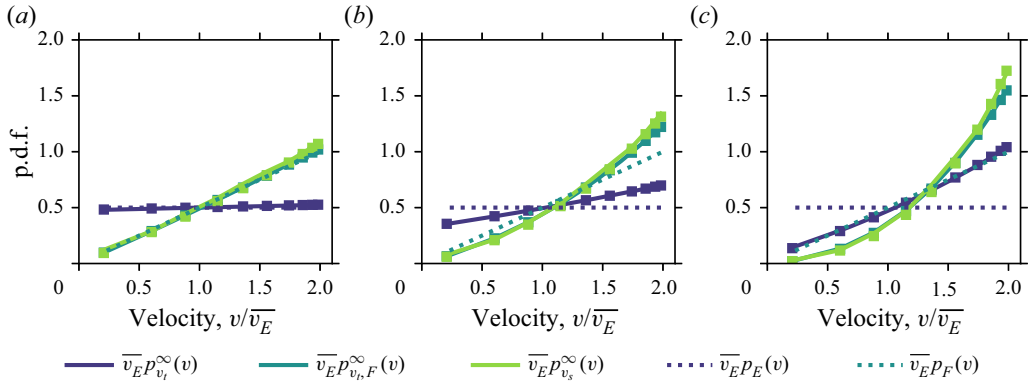
985 A16-21

Figure 8. Equilibrium velocity p.d.f. at fixed time $p_{v_t}^\infty$, corresponding flux-weighted p.d.f. $p_{v_t,F}^\infty$, and breakthrough velocity p.d.f. $p_{v_s}^\infty$ in the 3-D channel, for (a) $Da = 10^{-1}$, (b) $Da = 1$, and (c) $Da = 10$. Symbols show the results of numerical simulations. The solid lines associated with $p_{v_t}^\infty$ and $p_{v_t,F}^\infty$ in (a,c) show the analytical limit forms (F13) and (F15) for low Da, and (F14) and (F16) for high Da. The corresponding solid lines in (b) show the analytical solutions (4.27) and (4.28), with μ_1 computed numerically according to (4.18b). The solid lines associated with $p_{v_s}^\infty$ use (3.27) in all plots, with p_s computed as in figure 7. Dotted lines show the Eulerian and flux-weighted Eulerian p.d.f.s, which equal $p_{v_t}^\infty$ and $p_{v_s}^\infty = p_{v_t,F}^\infty$ for the conservative problem.

5. Discussion and conclusions

We have provided a detailed analysis of the asymptotic transverse distributions of surviving mass, velocity and breakthrough fluxes for advective–diffusive transport in Poiseuille flow between two flat plates and in a cylindrical channel. Just as for the conservative case, asymptotic forms exist, even in the limit of instantaneous reaction. In addition to qualitatively intuitive changes associated with the depletion of low-velocity regions due to reaction at the channel walls, we have also found that the equality between flux-weighted and breakthrough quantities, as well as between the mean plume velocity and the average of the transverse velocity distribution at fixed time, are modified by the presence of reaction. These effects result from variability in the mean plume position over the channel cross-section, which, despite being of subleading order in time, contributes at leading order to the mean plume velocity and results in non-vanishing asymptotic effects. As we have seen, the effect of this mechanism on breakthrough distributions is noticeable but mild, especially in the two-dimensional case. The effect on the mean plume velocity is more substantial in both cases.

The simplicity of the set-up used here in terms of the geometry, flow profile and chemical kinetics allows most of the calculations to be carried out analytically. This elucidates the underlying mechanisms and also provides analytical building blocks that can be used to develop models that are applicable to more complex scenarios. In this context, the results raise a number of questions that remain open. Does the ordering under fast reaction, $\overline{v_E} < \overline{v_F} < v_t^\infty < v_{t,F}^\infty < v_s^\infty < v_P^\infty$, of the different mean velocities discussed here hold for arbitrary geometries? What geometric features lead to larger or smaller differences between the mean plume velocity and the average of the transverse velocity distribution, and between breakthrough and flux-weighted quantities? To what extent do these results affect the formal structure and predictions of stochastic models of transport based on velocity distributions, and how can they be adapted to account for more complex geometry, flow heterogeneity and rheology, as encountered, for example, in natural porous and fractured rock formations or in biological systems? Answering these questions, in

particular for the single channel and for ensembles of connected channels, will be the subject of future work.

Declaration of interests. The author reports no conflict of interest.

Author ORCIDs.
Tomás Aquino https://orcid.org/0000-0001-9033-7202.

Appendix A. Transverse quantities in terms of Aris–Barton moments

Here, we relate the transverse quantities introduced in §3 to moments in the classical Aris–Barton formulation (Barton 1984). To this end, we define the integral operators

$$
\left.\begin{aligned}
\mathrm{I}_x f = \int_0^\infty \mathrm{d}x\, f(x), \quad \mathrm{I}_\perp f = \int_{\Omega_\perp} \mathrm{d}\boldsymbol{x}_\perp f(\boldsymbol{x}_\perp), \\
\mathrm{I}_t f = \int_0^T \mathrm{d}t\, f(t), \quad \mathrm{I}_v f = \int_0^{v_M} f(v)\, \mathrm{d}v,
\end{aligned}\right\}
\tag{A1}
$$

where f is an arbitrary function that depends on the appropriate physical variable, and variables not affected by the operator are understood to be kept constant. We introduce the local axial moments

$$
C_m = \mathrm{I}_x \hat{x}^m c,
\tag{A2}
$$

where $m \in \mathbb{N}$, the hat indicates the identity function (i.e. $\hat{x}(x) = x$), and the global moments

$$
M_m = \mathrm{I}_\perp C_m.
\tag{A3}
$$

Note that $M_0(t) = M(t)$, the total mass at time t. An analytical treatment of these moments may be found in Barton (1984).

In terms of these definitions, the transverse mass p.d.f. is given by

$$
p_t = \frac{C_0}{M_0}.
\tag{A4a}
$$

Its flux-weighted counterpart is

$$
p_{t,F} = \frac{v_E p_t}{\mathrm{I}_\perp v_E p_t},
\tag{A4b}
$$

and the breakthrough p.d.f. is in turn

$$
p_s = \frac{\mathrm{I}_t v_E c}{\mathrm{I}_\perp \mathrm{I}_t v_E c}.
\tag{A4c}
$$

As discussed in the main text and in Appendix B, the velocity p.d.f.s associated with spatial sampling according to the previous p.d.f.s can be obtained through what amounts to a change of variables. That is,

$$
p_{v_t} = \mathrm{I}_\perp \delta_{v_E} p_t, \quad p_{v_t,F} = \mathrm{I}_\perp \delta_{v_E} p_{t,F}, \quad p_{v_s} = \mathrm{I}_\perp \delta_{v_E} p_s,
\tag{A5a-c}
$$

where δ_{v_E} is the Dirac delta centred at v_E, $\delta_{v_E(\boldsymbol{x}_\perp)}(v) = \delta[v_E(\boldsymbol{x}_\perp) - v]$. At equilibrium, when from symmetry considerations the transverse mass p.d.f.s must be a function of

radial position only, this simplifies to

$$p_{v_t}^\infty = p_t(r_\perp)\, p_E, \quad p_{v_t,F}^\infty = p_{t,F}^\infty(r_\perp)\, p_E, \quad p_{v_s}^\infty = p_s^\infty(r_\perp)\, p_E; \tag{A6a–c}$$

see (3.7). For the corresponding mean velocities, we have

$$v_t = \mathrm{I}_v \hat{v} p_{v_t} = \mathrm{I}_\perp v_E p_t, \tag{A7a}$$

$$v_{t,F} = \mathrm{I}_v \hat{v} p_{v_t,F} = \mathrm{I}_\perp v_E^2 p_t, \tag{A7b}$$

$$v_s = \mathrm{I}_v \hat{v} p_{v_s} = \mathrm{I}_\perp v_E p_s. \tag{A7c}$$

Finally, the mean plume velocity is the rate of change of the mean plume position,

$$v_P = \frac{\mathrm{d}m_P}{\mathrm{d}t}, \quad m_P = \frac{M_1}{M_0}, \tag{A8a,b}$$

and we have for the transverse-position-dependent mean position:

$$m = \frac{C_1}{C_0}, \tag{A9}$$

so that from (3.15),

$$v_P^\infty = v_t^\infty + \alpha^\infty \lim_{t \to \infty} \left(\frac{M_1}{M_0} - \frac{C_1}{C_0}\bigg|_{\boldsymbol{x}_\perp \in \partial \Omega_\perp} \right). \tag{A10}$$

Appendix B. Flow velocity distributions

In this appendix, we provide details on the Eulerian and flux-weighted p.d.f.s associated with flow velocity at fixed times, and their relationship with the velocity p.d.f. characterizing advective velocities at fixed time. The Eulerian velocity p.d.f. is defined as the probability density associated with finding a certain velocity magnitude value at a uniformly random spatial location,

$$p_E(v) = |\Omega_\perp|^{-1} \int_{\Omega_\perp} \mathrm{d}\boldsymbol{x}_\perp \, \delta[v - v_E(\boldsymbol{x}_\perp)], \tag{B1}$$

where $\delta(\cdot)$ is the Dirac delta. In order to express this p.d.f. in a more practical form, it is convenient to change variables in the integrand to explicitly use the fact that the contributions to $p_E(v)$ arise from positions $\boldsymbol{x}_\perp$ where the velocity has a specified value v. The Dirac delta can be expressed as a simple layer integral (Hörmander 2015; Aquino & Le Borgne 2021b)

$$\delta[v - v_E(\boldsymbol{x}_\perp)] = \int_{\Lambda(v)} \mathrm{d}\boldsymbol{x}_\perp' \, \frac{\delta(\boldsymbol{x}_\perp' - \boldsymbol{x}_\perp)}{|\boldsymbol{\nabla}_\perp v_E(\boldsymbol{x}_\perp'; t)|}, \tag{B2}$$

where $\Lambda(v)$ is the $(d-2)$-surface of points $\boldsymbol{x}_\perp$ where $v_E(\boldsymbol{x}_\perp) = v$. For channel flow, the shear rate magnitude as a function of velocity $\alpha(v) = |\boldsymbol{\nabla}_\perp v_E(\boldsymbol{x}_\perp; t)|_{\boldsymbol{x}_\perp \in \Lambda(v)}$ is well defined, as it is constant over surfaces of constant velocity. Thus, substituting in (B2), we

985 A16-24

d	$|\Lambda(v)|$	$p_E(v)$	$p_F(v)$	$\overline{v_E}$	$\overline{v_F}$
2	2	$\dfrac{1}{2v_M\sqrt{1-v/v_M}}$	$\dfrac{3v}{4v_M^2\sqrt{1-v/v_M}}$	$2v_M/3$	$6\overline{v_E}/5$
3	$2\pi a\sqrt{1-\dfrac{v}{v_M}}$	$1/v_M$	$2v/v_M^2$	$v_M/2$	$4\overline{v_E}/3$

Table 2. Eulerian and flux-weighted Eulerian flow velocity p.d.f.s and associated quantities for Poiseuille flow between two flat plates (spatial dimension $d = 2$) and in a cylindrical channel ($d = 3$).

obtain

$$p_E(v) = \frac{|\Lambda(v)|}{|\Omega_\perp|\,\alpha(v)}. \tag{B3}$$

Note that the surface $\Lambda(v)$ of constant velocity is composed of points of constant radial coordinate $r_\perp(v) = |\boldsymbol{x}_\perp|$ given by

$$r_\perp(v) = a\sqrt{1 - \frac{v}{v_M}}. \tag{B4}$$

Recall that a is the channel radius and v_M is the maximum velocity, which occurs at the centre of the channel. For example, in two dimensions, this occurs at two points for $v \in {]0, v_M[}$, so that $|\Lambda(v)| = 2H(v_M - v)\,H(v)$, where H is the Heaviside step function. In what follows, we omit such Heaviside step functions for notational simplicity. Taking the derivative of the Poiseuille flow profile (2.2) with respect to $|\boldsymbol{x}_\perp|$ and substituting (B4),

$$\alpha(v) = \frac{2v_M}{a}\sqrt{1 - \frac{v}{v_M}}. \tag{B5}$$

We also define the flux-weighted Eulerian p.d.f. $p_F(v) = v\,p_E(v)/\overline{v_E}$. Some useful quantities relating to p_E and p_F and their means $\overline{v_E}$ and $\overline{v_F}$ for Poiseuille flow in two and three dimensions, computed according to these results, are summarized in table 2.

We can now generalize the discussion above leading to the Eulerian p.d.f. The transverse velocity p.d.f. at fixed time $p_{v_t}^\infty(\cdot; t)$ is obtained by sampling spatial locations according to the p.d.f. $p_t(\cdot; t)$ of cross-section positions determined by the surviving mass profile, rather than uniformly. That is,

$$p_{v_t}(v; t) = \int_{\Omega_\perp} \mathrm{d}\boldsymbol{x}_\perp\, p_t(\boldsymbol{x}_\perp; t)\,\delta[v - v_E(\boldsymbol{x}_\perp)]. \tag{B6}$$

Using (B2), together with the fact that the shear rate $\alpha(v)$ is constant over surfaces of constant v, we obtain

$$p_{v_t}(v; t) = |\alpha(v)|^{-1} \int_{\Lambda(v)} \mathrm{d}\boldsymbol{x}_\perp\, p_t(\boldsymbol{x}_\perp; t). \tag{B7}$$

From symmetry considerations, if the asymptotic surviving mass p.d.f. p_t^∞ exists, then it must depend only on the radial coordinate, and therefore can also be expressed as a function of velocity through $r_\perp(v)$; see (B4). Thus, from (B3) and (B7),

$$p_{v_t}^\infty(v) = |\Omega_\perp|\,p_t^\infty(\boldsymbol{x}_\perp)|_{|\boldsymbol{x}_\perp|=r_\perp(v)}. \tag{B8}$$
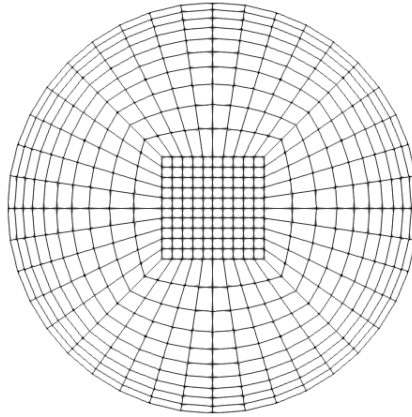
985 A16-25

Figure 9. Cross-section of the 3-D-channel mesh.

Appendix C. Numerical simulations

Numerical simulations of the reactive transport problem used in the text were performed using a standard second-order finite-volume solver in OpenFOAM (OpenCFD Ltd 2022). The mean Eulerian velocity was set to $\overline{v_E} = 1$, the domain radius (half-width in two dimensions) to $a = 1$, and the diffusion coefficient to $D = 1/2$. A flux-weighted pulse injection one discretization cell wide near $x = x_0 = 10$ was used in all simulations. The channel inlet was placed at $x = 0$, and the outlet at $x = 100$. The normalized equilibrium results presented in the text are not affected by these parameter and initial condition choices, except for the value of Péclet number $Pe = 2$ (defined according to (2.3)) in the case of breakthrough quantities. The boundary conditions at the inlet and outlet of the channel were absorbing, although care was taken to verify that no mass left the domain by the inlet or outlet within the times of interest. The Robin boundary condition (2.7) was imposed at the channel walls. The simulations were run up to time $t = 100$. Damköhler numbers $Da = 10^{-1}$, 1 and 10, defined according to (2.8a–c), were simulated.

For the 2-D channel, we employed a regular grid discretization with 1000 cells in the x direction and 20 cells in the y direction. For the 3-D channel, we used a regular discretization in a square central region of side $1/2$ to avoid numerical issues at the centre of the channel, as shown in figure 9. The discretization along the x direction was again regular using 1000 cells. Along each of the y and z directions, 30 cells were used: 10 in the square central region, and 10 on each side. The outer regions employed an expansion ratio of 25 %, such that cells decreased in size towards the channel wall from the centre.

The equilibrium profiles were evaluated at times τ and longitudinal positions $x_0 + \overline{v_E}\tau$. For the 2-D case, $\tau = 30$ for all values of Da. For the 3-D case, $\tau = 20$ for $Da = 10^{-1}$, and $\tau = 5$ for $Da = 1$ and $Da = 10$. These smaller values of τ in the latter cases were used to avoid numerical issues due to very small concentration values, which affect the computation of breakthrough fluxes at large distances. In addition, in these two cases, the initial mass was multiplied by a large value to avoid errors associated with roundoff procedures employed by OpenFOAM to prevent overflow on division by small numbers. This does not affect the results after normalizing by mass because the problem is linear.

Surviving mass p.d.f.s p_t are computed by integrating concentrations numerically over the longitudinal direction at the time of interest, using the underlying grid discretization. The breakthrough profiles p_s are computed by integrating concentrations multiplied by

local velocities over time at the longitudinal position of interest, using an integration time step 0.1. Mean plume velocities v_P^∞ are obtained by numerically computing the mean longitudinal position $m_P(t)$ at time $t = 40$, and estimating $v_P^\infty = [m_P(t) - x_0]/t$. The remaining mean velocities discussed in the text, v_t^∞, $v_{t,F}^\infty$ and v_s^∞, are obtained by direct numerical integration according to the relevant numerically determined p.d.f.s.

Appendix D. Asymptotic decay rate in terms of first passage times

As shown in the present work, the asymptotic reaction rate α^∞ associated with the decay of total plume mass at late times is constant and determined by the slowest decay mode of concentration,

$$\alpha^\infty = \frac{\mu_1^2}{2\tau_D}. \tag{D1}$$

Recently, the decay of total mass has been described in terms of first passage and return times to the reactive interface (Aquino & Le Borgne 2021*a*; Aquino *et al.* 2023). In particular, for an instantaneous injection of initial mass M_0 in the 2-D channel, it is given in Laplace space by (Aquino & Le Borgne 2021*a*)

$$\frac{\tilde{M}(\lambda)}{M_0} = \frac{2\,Da\,\tilde{\Psi}_0(\lambda) + \tanh(\sqrt{2\tau_D\lambda})\,\sqrt{2\tau_D/\lambda}}{2\,Da + \tanh(\sqrt{2\tau_D\lambda})\,\sqrt{2\tau_D\lambda}}, \tag{D2}$$

where the tilde denotes the Laplace transform, λ is the Laplace variable conjugate to time, and Ψ_0 is the survival probability, i.e. $\Psi_0(t)$ is the probability that first passage to the channel wall has not occurred by time t for a given initial concentration distribution in the channel. The description in terms of first passage times is particularly intuitive for $Da \to \infty$, which corresponds to fully-absorbing walls. Then, for any geometry, the total mass is fully determined by the first passage times and is given by $M(t) = M_0\,\Psi_0(t)$, i.e. the surviving mass is precisely the mass that has not yet reached the walls. The general result agrees with that reported in Zhang *et al.* (2017) for the case of a homogeneous initial distribution, for which $\tilde{\Psi}_0(\lambda) = [1 - \tanh(\sqrt{2\tau_D\lambda})/\sqrt{2\tau_D\lambda}]/\lambda$.

From (D2), the late-time reaction rate can be estimated by expanding for small λ, yielding (Aquino & Le Borgne 2021*a*)

$$\alpha^\infty = \frac{1 + Da\,w_0/\tau_D}{1 + Da\,(2/3 + w_0/\tau_D) + Da^2\,s_0^2/(2\tau_D^2)}\,\frac{Da}{\tau_D}, \tag{D3}$$

where w_0 is the mean first passage time, and s_0^2 is the corresponding second moment. This result differs from (D1) and appears to suggest that the late-time reaction rate depends on the initial mass distribution. The reason for this discrepancy is that the small-λ expansion of the Laplace transform of a function with a finite first moment produces an approximation of the late-time behaviour that recovers the correct first moment, rather than providing the exact late-time decay. This approximation becomes exact when the original function is itself exponential. For common initial distributions, such as a uniform injection, a flux-weighted injection ($\tilde{\Psi}_0(\lambda) = [1 - 3(1 - \tanh(\sqrt{2\tau_D\lambda})/\sqrt{2\tau_D\lambda})/(2\tau_D\lambda)]/\lambda$), or a mid-channel injection ($\tilde{\Psi}_0(\lambda) = [1 - \text{sech}(\sqrt{2\tau_D\lambda})]/\lambda$), the exponential approximation is sound and leads to maximum relative errors of approximately 1 %, 0.1 % and 3 %, respectively, which occur at infinite Da. Thus while it may wrongly suggest that the late-time behaviour is initial-condition-dependent, the Laplace expansion approach based

on the first passage time picture provides good approximations and generalizes well to more complex geometries (Aquino & Le Borgne 2021*a*; Aquino *et al.* 2023). This also shows that since for $Da \to \infty$ we have α^∞ independent of the initial condition, the actual late-time tail of the first passage time distribution is independent of the initial mass distribution and is instead fully determined by the diffusion coefficient and the geometry of the problem.

Appendix E. Damköhler expansions for the 2-D channel

In this appendix, we derive limiting forms for low and high Damöhler number *Da* of some of the equilibrium quantities discussed in the main text for the 2-D channel.

E.1. *Surviving mass*

First, consider the slowest concentration decay mode μ_1. For $Da \ll 1$, we can Taylor expand the second form in (4.1*e*) around $\mu = 0$, to obtain

$$\mu_1 \approx \sqrt{2\,Da}\left(1 - \frac{Da}{3} + \frac{11}{90}\,Da^2\right). \tag{E1}$$

In the opposite limit of fast reaction, $Da \gg 1$, we expand (4.1*d*) around $\mu = \pi/2$ and $1/Da = 0$ to obtain

$$\mu_1 \approx \frac{\pi}{2}\left(1 - \frac{1}{2\,Da}\right). \tag{E2}$$

Substituting (E1) in (4.3) and Taylor expanding for $Da \ll 1$ yields for the surviving mass p.d.f.

$$|\Omega_\perp|\,p_t^\infty(y) \approx 1 + \left(1 - \frac{3y^2}{a^2}\right)\frac{Da}{3}. \tag{E3}$$

In particular, note that $p_t^\infty(y) = 1/|\Omega_\perp| = 1/(2a)$ for $Da = 0$, as expected. Similarly, substituting (E2) and expanding for $Da \gg 1$ leads to

$$|\Omega_\perp|\,p_t^\infty(y) \approx \frac{\pi}{2}\cos\left(\frac{\pi y}{2a}\right)\left(1 - \left[1 - \frac{\pi y}{2a}\tan\left(\frac{\pi y}{2a}\right)\right]\frac{1}{2\,Da}\right). \tag{E4}$$

The corresponding flux-weighted p.d.f. (4.5) is, for low *Da*,

$$|\Omega_\perp|\,p_{t,F}^\infty(y) \approx \frac{3}{2}\left(1 - \frac{y^2}{a^2}\right)\left[1 + \left(1 - \frac{5y^2}{a^2}\right)\frac{Da}{5}\right], \tag{E5}$$

and, for high *Da*,

$$|\Omega_\perp|\,p_{t,F}^\infty(y) \approx \frac{\pi^3}{16}\left(1 - \frac{y^2}{a^2}\right)\cos\left(\frac{\pi y}{2a}\right)\left(1 - \left[3 - \frac{\pi^2}{4} - \frac{\pi y}{2a}\tan\left(\frac{\pi y}{2a}\right)\right]\frac{1}{2\,Da}\right). \tag{E6}$$

E.2. *Velocity*

For $Da \ll 1$, we obtain the average of the fixed-time velocity p.d.f. (4.13),

$$\frac{v_t^\infty}{\overline{v_E}} \approx 1 + \frac{2\,Da}{15} - \frac{4\,Da^2}{63}. \tag{E7}$$

In particular, we recover $v_t^\infty = \overline{v_E}$ for the conservative problem, as expected. Note that in order to obtain this result to second order in *Da* with the expansion (E1) for μ_1, it is

985 A16-28

necessary to use the first form in (4.13); for the second form, a higher-order expansion of μ_1 in Da would be necessary. The second-order accuracy is necessary to achieve first-order accuracy in $v_{t,F}^\infty$ below. For $Da \gg 1$, we have

$$\frac{v_t^\infty}{\overline{v_E}} \approx \frac{12}{\pi^2} \left(1 - \frac{\pi^2 - 8}{8\,Da} \right). \tag{E8}$$

For the mean plume velocity (4.14), we find, for $Da \ll 1$,

$$\frac{v_P^\infty}{\overline{v_E}} \approx 1 + \frac{4\,Da}{15}, \tag{E9}$$

and, for $Da \gg 1$,

$$\frac{v_P^\infty}{\overline{v_E}} \approx 1 + \frac{3}{\pi^2} - \left(\frac{1}{2} - \frac{3}{\pi^2} \right) \frac{1}{Da}. \tag{E10}$$

For $Da \ll 1$, using (E1) and (E7), (4.15) for the flux-weighted average velocity reduces to

$$\frac{v_{t,F}^\infty}{\overline{v_F}} \approx 1 + \frac{2\,Da}{35}. \tag{E11}$$

Again as expected, we recover $v_{t,F}^\infty = \overline{v_F}$ in the conservative limit. For $Da \gg 1$,

$$\frac{v_{t,F}^\infty}{\overline{v_F}} \approx \frac{5}{\pi^2} \left(12 - \pi^2 - \frac{\pi^4 - 96}{8\,Da} \right). \tag{E12}$$

Proceeding similarly, the $Da \ll 1$ limit of (4.16) for the equilibrium fixed-time velocity p.d.f. is

$$\frac{p_{v_t}^\infty(v)}{p_E(v)} \approx 1 - \left(1 - \frac{v}{\overline{v_E}} \right) \frac{2\,Da}{3}, \tag{E13}$$

and for $Da \gg 1$ we have

$$\frac{p_{v_t}^\infty(v)}{p_E(v)} \approx \frac{\pi}{2} \cos\left(\frac{\pi}{2} \sqrt{1 - \frac{v}{v_M}} \right) \left(1 - \left[1 - \frac{\pi}{2} \sqrt{1 - \frac{v}{v_M}} \tan\left(\frac{\pi}{2} \sqrt{1 - \frac{v}{v_M}} \right) \right] \frac{1}{2\,Da} \right). \tag{E14}$$

For the equilibrium flux-weighted velocity p.d.f. (4.17), the low-Da limit is

$$\frac{p_{v_t,F}^\infty(v)}{p_F(v)} \approx 1 - \left(1 - \frac{v}{\overline{v_F}} \right) \frac{4\,Da}{5}, \tag{E15}$$

and for the high-Da limit, we obtain

$$\frac{p_{v_t,F}^\infty(v)}{p_F(v)} \approx \frac{\pi^3}{24} \cos\left(\frac{\pi}{2} \sqrt{1 - \frac{v}{v_M}} \right)$$
$$\times \left(1 - \left[3 - \frac{\pi^2}{4} - \frac{\pi}{2} \sqrt{1 - \frac{v}{v_M}} \tan\left(\frac{\pi}{2} \sqrt{1 - \frac{v}{v_M}} \right) \right] \frac{1}{2\,Da} \right). \tag{E16}$$

Appendix F. Damköhler expansions for the 3-D channel

Here, we derive limiting forms for low and high Damöhler number Da of some of the equilibrium quantities discussed in the main text for the 3-D channel.

F.1. *Surviving mass*

Expanding (4.18*b*) to sixth order in μ, solving for μ, and expanding for small *Da*, we find for the slowest concentration decay mode:

$$\mu_1 \approx 2\sqrt{Da}\left(1 - \frac{Da}{4} + \frac{5\,Da^2}{96}\right). \tag{F1}$$

For $Da \to \infty$, we have $J_0(\mu) = 0$, so that $\mu_1 = j_{0,1} \approx 2.4048$, the smallest positive root of J_0. Expanding μ to first order around this value in (4.18*b*), we obtain the high-*Da* expansion

$$\mu_1 \approx j_{0,1}\left(1 - \frac{1}{2\,Da}\right). \tag{F2}$$

Using (4.19) and (F1), we find the low-*Da* expansion for the surviving mass p.d.f.:

$$|\Omega_\perp|\,p_t^\infty(\boldsymbol{x}_\perp) \approx 1 + \left(1 - \frac{2\,|\boldsymbol{x}_\perp|^2}{a^2}\right)\frac{Da}{2}. \tag{F3}$$

Note that, as expected, in the conservative limit we recover a uniform transverse p.d.f. $p_t^\infty(\boldsymbol{x}_\perp) = 1/|\Omega_\perp| = 1/(\pi a^2)$. Based on (4.19) and (F2), we obtain the high-*Da* expansion

$$|\Omega_\perp|\,p_t^\infty(\boldsymbol{x}_\perp) \approx \frac{j_{0,1}\,J_0(j_{0,1}\,|\boldsymbol{x}_\perp|/a)}{2\,J_1(j_{0,1})}\left[1 - \left(1 - \frac{j_{0,1}\,J_1(j_{0,1}\,|\boldsymbol{x}_\perp|/a)}{2\,J_0(j_{0,1}\,|\boldsymbol{x}_\perp|/a)}\,\frac{|\boldsymbol{x}_\perp|}{a}\right)\frac{1}{Da}\right]. \tag{F4}$$

Correspondingly, for the flux-weighted p.d.f., we find for low *Da*

$$|\Omega_\perp|\,p_{t,F}^\infty(\boldsymbol{x}_\perp) \approx 2\left(1 - \frac{|\boldsymbol{x}_\perp|^2}{a^2}\right)\left[1 + \left(1 - \frac{3\,|\boldsymbol{x}_\perp|^2}{a^2}\right)\frac{Da}{3}\right], \tag{F5}$$

and for high *Da*,

$$\begin{aligned}
|\Omega_\perp|\,p_{t,F}^\infty(\boldsymbol{x}_\perp) &\approx \frac{j_{0,1}^3\,J_0(j_{0,1}\,|\boldsymbol{x}_\perp|/a)}{8\,J_1(j_{0,1})}\left(1 - \frac{|\boldsymbol{x}_\perp|^2}{a^2}\right) \\
&\quad \times \left[1 - \left(8 - j_{0,1}^2 - \frac{2j_{0,1}\,J_1(j_{0,1}\,|\boldsymbol{x}_\perp|/a)}{J_0(j_{0,1}\,|\boldsymbol{x}_\perp|/a)}\,\frac{|\boldsymbol{x}_\perp|}{a}\right)\frac{1}{4\,Da}\right].
\end{aligned} \tag{F6}$$

F.2. *Velocity*

The average of the fixed-time velocity p.d.f. (4.24), admits the low-*Da* expansion

$$\frac{v_t^\infty}{v_E} \approx 1 + \frac{Da}{6} - \frac{Da^2}{24}, \tag{F7}$$

and the high-*Da* expansion

$$\frac{v_t^\infty}{v_E} \approx \frac{8}{j_{0,1}^2}\left(1 - \frac{j_{0,1}^2 - 4}{4\,Da}\right). \tag{F8}$$

For the plume velocity (4.25), we find for $Da \ll 1$,

$$\frac{v_P^\infty}{v_E} \approx 1 + \frac{Da}{3}, \tag{F9}$$

and for $Da \gg 1$,

$$\frac{v_P^\infty}{\overline{v_E}} \approx \frac{4}{3} \left(1 + \frac{1}{j_{0,1}^2} \right) - \left(1 - \frac{2}{j_{0,1}^2} \right) \frac{2}{3\,Da}. \tag{F10}$$

Note that these approximations agree with those reported in Sankarasubramanian & Gill (1973) and Barton (1984) to the relevant order in Da.

For $Da \ll 1$, we obtain the flux-weighted average velocity (4.26),

$$\frac{v_{t,F}^\infty}{\overline{v_F}} \approx 1 + \frac{Da}{12}, \tag{F11}$$

and, for $Da \gg 1$,

$$\frac{v_{t,F}^\infty}{\overline{v_F}} \approx 3 \frac{8 - j_{0,1}^2}{j_{0,1}^2} \left(1 - \frac{j_{0,1}^4 - 32}{8 - j_{0,1}^2} \frac{1}{4\,Da} \right). \tag{F12}$$

For the equilibrium fixed-time velocity p.d.f. (4.27), we have for low Da,

$$\frac{p_{v_t}^\infty(v)}{p_E(v)} \approx 1 - \left(1 - \frac{v}{\overline{v_E}} \right) \frac{Da}{2}, \tag{F13}$$

and for high Da,

$$\frac{p_{v_t}^\infty(v)}{p_E(v)} \approx \frac{j_{0,1}\,\mathrm{J}_0(j_{0,1}\sqrt{1 - v/v_M})}{2\,\mathrm{J}_1(j_{0,1})} \left[1 - \left(1 - \frac{j_{0,1}\,\mathrm{J}_1(j_{0,1}\sqrt{1 - v/v_M})}{2\,\mathrm{J}_0(j_{0,1}\sqrt{1 - v/v_M})} \sqrt{1 - \frac{v}{v_M}} \right) \frac{1}{Da} \right]. \tag{F14}$$

For the equilibrium flux-weighted velocity p.d.f. (4.28), the low-Da limit is

$$\frac{p_{v_t,F}^\infty(v)}{p_F(v)} \approx 1 - \left(1 - \frac{v}{\overline{v_F}} \right) \frac{2\,Da}{3}, \tag{F15}$$

and the high-Da limit is

$$\frac{p_{v_t,F}^\infty(v)}{p_F(v)} \approx \frac{j_{0,1}^3\,\mathrm{J}_0(j_{0,1}\sqrt{1 - v/v_M})}{16\,\mathrm{J}_1(j_{0,1})}$$

$$\times \left[1 - \left(8 - j_{0,1}^2 - \frac{2 j_{0,1}\,\mathrm{J}_1(j_{0,1}\sqrt{1 - v/v_M})}{\mathrm{J}_0(j_{0,1}\sqrt{1 - v/v_M})} \sqrt{1 - \frac{v}{v_M}} \right) \frac{1}{4\,Da} \right]. \tag{F16}$$

REFERENCES

ABRAMOWITZ, M. & STEGUN, I.A. 1964 *Handbook of Mathematical Functions with Formulas, Graphs, and Mathematical Tables*. Dover.

AQUINO, T. & LE BORGNE, T. 2021*a* The chemical continuous time random walk framework for upscaling transport limitations in fluid–solid reactions. *Adv. Water Resour.* **154**, 103981.

AQUINO, T. & LE BORGNE, T. 2021*b* The diffusing-velocity random walk: a spatial-Markov formulation of heterogeneous advection and diffusion. *J. Fluid Mech.* **910**, A12.

AQUINO, T., LE BORGNE, T. & HEYMAN, J. 2023 Fluid–solid reaction in porous media as a chaotic restart process. *Phys. Rev. Lett.* **130** (26), 264001.

ARIS, R. 1956 On the dispersion of a solute in a fluid flowing through a tube. *Proc. R. Soc. Lond.* A **235** (1200), 67–77.

BALAKOTAIAH, V., CHANG, H.-C. & SMITH, F.T. 1995 Dispersion of chemical solutes in chromatographs and reactors. *Phil. Trans. R. Soc. Lond.* A **351** (1695), 39–75.

BARTON, N.G. 1983 On the method of moments for solute dispersion. *J. Fluid Mech.* **126**, 205–218.

BARTON, N.G. 1984 An asymptotic theory for dispersion of reactive contaminants in parallel flow. *ANZIAM J.* **25** (3), 287–310.

BATTIATO, I., TARTAKOVSKY, D.M., TARTAKOVSKY, A.M. & SCHEIBE, T.D. 2011 Hybrid models of reactive transport in porous and fractured media. *Adv. Water Resour.* **34** (9), 1140–1150.

BISWAS, R.R. & SEN, P.N. 2007 Taylor dispersion with absorbing boundaries: a stochastic approach. *Phys. Rev. Lett.* **98** (16), 164501.

CARSLAW, H.S. & JAEGER, J.C. 1986 *Conduction of Heat in Solids*, 2nd edn. Oxford University Press.

CHATWIN, P.C. 1970 The approach to normality of the concentration distribution of a solute in a solvent flowing along a straight pipe. *J. Fluid Mech.* **43** (2), 321–352.

DAVIDSON, M.R. & SCHROTER, R.C. 1983 A theoretical model of absorption of gases by the bronchial wall. *J. Fluid Mech.* **129**, 313–335.

DE GANCE, A.E. & JOHNS, L.E. 1978*a* On the dispersion coefficients for Poiseuille flow in a circular cylinder. *Flow Turbul. Combust.* **34**, 227–258.

DE GANCE, A.E. & JOHNS, L.E. 1978*b* The theory of dispersion of chemically active solutes in a rectilinear flow field. *Flow Turbul. Combust.* **34**, 189–225.

DENTZ, M., KANG, P.K., COMOLLI, A., LE BORGNE, T. & LESTER, D.R. 2016 Continuous time random walks for the evolution of Lagrangian velocities. *Phys. Rev. Fluids* **1** (7), 074004.

DEWHIRST, M.W. & SECOMB, T.W. 2017 Transport of drugs from blood vessels to tumour tissue. *Nat. Rev. Cancer* **17** (12), 738–750.

GOIRAND, F., LE BORGNE, T. & LORTHOIS, S. 2021 Network-driven anomalous transport is a fundamental component of brain microvascular dysfunction. *Nat. Commun.* **12** (1), 7295.

GRITTI, F. & GUIOCHON, G. 2013 Perspectives on the evolution of the column efficiency in liquid chromatography. *Anal. Chem.* **85** (6), 3017–3035.

GUAN, M. & CHEN, G. 2024 Streamwise dispersion of soluble matter in solvent flowing through a tube. *J. Fluid Mech.* **980**, A33.

HEINZE, T. 2021 Constraining the heat transfer coefficient of rock fractures. *Renew. Energy* **177**, 433–447.

HÖRMANDER, L. 2015 *The Analysis of Linear Partial Differential Operators I: Distribution Theory and Fourier Analysis*. Springer.

IVANOV, K.P., KALININA, M.K. & LEVKOVICH, Y.I. 1981 Blood flow velocity in capillaries of brain and muscles and its physiological significance. *Microvasc. Res.* **22** (2), 143–155.

JIANG, W., ZENG, L., FU, X. & WU, Z. 2022 Analytical solutions for reactive shear dispersion with boundary adsorption and desorption. *J. Fluid Mech.* **947**, A37.

LE BORGNE, T., DENTZ, M. & CARRERA, J. 2008 Lagrangian statistical model for transport in highly heterogeneous velocity fields. *Phys. Rev. Lett.* **101** (9), 090601.

LUNGU, E.M. & MOFFATT, H.K. 1982 The effect of wall conductance on heat diffusion in duct flow. *J. Engng Maths* **16** (2), 121–136.

DE MARSILY, G. 1986 *Quantitative Hydrogeology*. Academic.

MIKELIĆ, A., DEVIGNE, V. & VAN DUIJN, C.J. 2006 Rigorous upscaling of the reactive flow through a pore, under dominant Péclet and Damkohler numbers. *SIAM J. Math. Anal.* **38** (4), 1262–1287.

OPENCFD LTD 2022 Open-source CFD software OpenFOAM, version v2206. https://www.openfoam.com/.

PAINE, M.A., CARBONELL, R.G. & WHITAKER, S. 1983 Dispersion in pulsed systems – I: heterogenous reaction and reversible adsorption in capillary tubes. *Chem. Engng Sci.* **38** (11), 1781–1793.

POLYANIN, A.D. & NAZAIKINSKII, V.E. 2016 *Handbook of Linear Partial Differential Equations for Engineers and Scientists*, 2nd edn. CRC.

PUYGUIRAUD, A., GOUZE, P. & DENTZ, M. 2021 Pore-scale mixing and the evolution of hydrodynamic dispersion in porous media. *Phys. Rev. Lett.* **126** (16), 164501.

SANKARASUBRAMANIAN, R. & GILL, W.N. 1973 Unsteady convective diffusion with interphase mass transfer. *Proc. Math. Phys. Engng Sci.* **333** (1592), 115–132.

SHAPIRO, M. & BRENNER, H. 1986 Taylor dispersion of chemically reactive species: irreversible first-order reactions in bulk and on boundaries. *Chem. Engng Sci.* **41** (6), 1417–1433.

SHERMAN, T., ENGDAHL, N.B., PORTA, G. & BOLSTER, D. 2021 A review of spatial Markov models for predicting pre-asymptotic and anomalous transport in porous and fractured media. *J. Contam. Hydrol.* **236**, 103734.

SHERMAN, T., PASTER, A., PORTA, G. & BOLSTER, D. 2019 A spatial Markov model for upscaling transport of adsorbing–desorbing solutes. *J. Contam. Hydrol.* **222**, 31–40.

SZNITMAN, J. 2021 Revisiting airflow and aerosol transport phenomena in the deep lungs with microfluidics. *Chem. Rev.* **122** (7), 7182–7204.

TAYLOR, G.I. 1953 Dispersion of soluble matter in solvent flowing slowly through a tube. *Proc. Math. Phys. Engng Sci.* **219** (1137), 186–203.

YASUDA, H. 1984 Longitudinal dispersion of matter due to the shear effect of steady and oscillatory currents. *J. Fluid Mech.* **148**, 383–403.

ZHANG, L., HESSE, M.A. & WANG, M. 2017 Transient solute transport with sorption in Poiseuille flow. *J. Fluid Mech.* **828**, 733–752.